

1 **Aircraft Measurements of Gravity Waves in the Upper Troposphere and Lower**
2 **Stratosphere during the START08 Field Experiment**

3
4 Fuqing Zhang^{1*}, Junhong Wei¹, Meng Zhang¹, Kenneth P. Bowman², Laura L. Pan³, Elliot
5 Atlas⁴, and Steve C. Wofsy⁵

- 6
7 1. Department of Meteorology, The Pennsylvania State University, University Park,
8 Pennsylvania
9 2. Department of Atmospheric Sciences, Texas A&M University, College Station, Texas
10 3. National Center for Atmospheric Research, Boulder, Colorado
11 4. Rosenstiel School of Marine and Atmospheric Science, University of Miami, Miami,
12 Florida
13 5. Division of Engineering and Applied Science/Department of Earth and Planetary
14 Science, Harvard University, Cambridge, Massachusetts

15
16
17 **Submitted to *Atmospheric Chemistry and Physics* for publication**

18 **Initial Submission, 3 November 2014**

19 **Revised submission, 28 December 2014**

20 **Final revision, 27 May 2015**

21
22

Corresponding author address: Professor Fuqing Zhang, Dept. of Meteorology, The Pennsylvania State University, University Park, PA 16802. E-mail: fzhang@psu.edu

23
24
25
26
27
28
29
30
31
32
33
34
35
36
37
38
39
40
41
42
43
44
45
46

Abstract

This study analyzes *in-situ* airborne measurements from the 2008 Stratosphere-Troposphere Analyses of Regional Transport (START08) experiment to characterize gravity waves in the extratropical upper troposphere and lower stratosphere (ExUTLS). The focus is on the second research flight (RF02), which took place on 21-22 April 2008. This was the first airborne mission dedicated to probing gravity waves associated with strong upper-tropospheric jet-front systems. Based on spectral and wavelet analyses of the *in-situ* observations, along with a diagnosis of the polarization relationships, clear signals of mesoscale variations with wavelengths ~ 50 - 500 km are found in almost every segment of the 8-hr flight, which took place mostly in the lower stratosphere. The aircraft sampled a wide range of background conditions including the region near the jet core, the jet exit and over the Rocky Mountains with clear evidence of vertically propagating gravity waves of along-track wavelength between 100 and 120 km. The power spectra of the horizontal velocity components and potential temperature for the scale approximately between ~ 8 km and ~ 256 km display an approximate $-5/3$ power law in agreement with past studies on aircraft measurements, while the fluctuations roll over to a -3 power law for the scale approximately between ~ 0.5 km and ~ 8 km (except when this part of the spectrum is activated, as recorded clearly by one of the flight segments). However, at least part of the high-frequency signals with sampled periods of ~ 20 - ~ 60 seconds and wavelengths of ~ 5 - ~ 15 km might be due to intrinsic observational errors in the aircraft measurements, even though the possibilities that these fluctuations may be due to other physical phenomena (e.g., nonlinear dynamics, shear instability and/or turbulence) cannot be completely ruled out.

47 **1. Introduction**

48 One of the challenges to understanding the extratropical upper troposphere and lower
49 stratosphere (ExUTLS) is that dynamical processes with a wide range of scales occur in the
50 region. Gravity waves, in particular, are known to play a significant role in determining the
51 structure and composition of the ExUTLS. Tropopause jets and fronts are significant sources of
52 gravity waves (O’Sullivan and Dunkerton 1995; Reeder and Griffins 1996; Zhang 2004; Wang
53 and Zhang 2007; Mirzaei et al. 2014; Wei and Zhang 2014, 2015), along with surface
54 topography (Smith 1980) and moist convection (Lane et al. 2001). Gravity waves above the jet
55 may be responsible for double or multiple tropopauses (Yamanaka et al. 1996; Pavelin et al.
56 2001) and may contribute to layered ozone or PV structures (Bertin et al. 2001). Also, strong
57 horizontal and vertical shear in the layer and the discontinuity in static stability at the tropopause
58 provide a favorable environment to reflect, capture, break and dissipate gravity waves generated
59 in the lower troposphere, such as those produced by surface fronts (Plougonven and Snyder
60 2007). Gravity wave breaking and wave-induced turbulence (e.g., Koch et al. 2005) can
61 contribute significantly to mixing of trace gases in the ExUTLS, thereby affecting chemical
62 composition (Vaughan and Worthington, 2000). Also, convectively-generated gravity waves
63 may extend the impact of moist convection far above cloud tops through wave-induced mixing
64 and transport (Lane et al. 2004).

65 In particular, mesoscale gravity waves with horizontal wavelength of $\sim 50\text{--}500$ km are
66 known to occur in the vicinity of unbalanced upper-tropospheric jet streaks and on the cold-air
67 side of surface frontal boundaries (Uccellini and Koch 1987; Plougonven and Zhang 2014). This
68 phenomenon has been identified repeatedly in both observational studies (Uccellini and Koch
69 1987; Schneider 1990; Fritts and Nastrom 1992; Ramamurthy et al. 1993; Bosart et al. 1998;

70 Koppel et al. 2000; Rauber et al. 2001; Plougonven et al. 2003) and numerical investigations of
71 the observed cases (Powers and Reed 1993; Pokrandt et al. 1996; Kaplan et al. 1997; Zhang and
72 Koch 2000; Zhang et al. 2001, 2003; Koch et al. 2001, 2005; Lane et al. 2004). In addition,
73 idealized simulations of dry baroclinic jet-front systems in a high-resolution mesoscale model
74 have been performed to investigate the generation of mesoscale gravity waves (Zhang 2004), the
75 sensitivity of mesoscale gravity waves to the baroclinicity of jet-front systems (Wang and Zhang
76 2007), and the source of gravity waves with multiple horizontal scales (Lin and Zhang 2008).
77 Most recently, Wei and Zhang (2014, 2015) studied the characteristics and potential source
78 mechanisms of mesoscale gravity waves in moist baroclinic jet-front systems with varying
79 degree of convective instability.

80 Advances in space technology provide the means to observe gravity waves in detail.
81 Recent studies have demonstrated that satellites such as Microwave Limb Sounder (MLS) and
82 Advanced Microwave Sounding Unit-A (AMSU-A) offer quantitative information of gravity
83 waves in the middle atmosphere (Alexander and Rosenlof 2003; Wu and Zhang 2004; Zhang et
84 al. 2013). In addition to satellite measurements, gravity waves are also observed by surface
85 observations (Einaudi et al. 1989; Grivet-Talocia et al. 1999; Koppel et al. 2000), high-resolution
86 radionsonde networks (Vincent and Alexander 2000; Wang and Geller 2003; Zhang and Yi
87 2007; Gong and Geller 2010), radars (Vaughan and Worthington 2000, 2007), and super-
88 pressure balloons (Hertzog and Vial 2001).

89 Among the abovementioned observational tools, aircraft have also been widely used as
90 *in-situ* measurements of gravity waves. Probably since Radok (1954), which was one of the first
91 observations of mountain waves with aircraft, past aircraft field campaigns have mainly focused
92 on terrain-induced gravity waves (Radok 1954; Vergeiner and Lilly 1970; Lilly and Kennedy

93 1973; Smith 1976; Karacostas and Marwitz 1980; Brown 1983; Moustouei et al. 1999;
94 Leutbecher and Volkert 2000; Poulos et al. 2002; Dornbrack et al. 2002; Doyle et al. 2002;
95 Smith et al. 2008). The recent Terrain-Induced Rotor Experiment (T-REX) in March-April 2006
96 (Grubišić et al. 2008) was the first full research project to use the National Science Foundation
97 (NSF) – National Center for Atmospheric Research (NCAR) Gulfstream V (GV) (Laursen et al.
98 2006), which has better Global Positioning System (GPS) accuracy than the previous versions.
99 The National Aeronautics and Space Administration (NASA) high-altitude ER-2 research
100 aircraft was also employed during the recent Cirrus Regional Study of Tropical Anvils and
101 Cirrus Layers Florida Area Cirrus Experiment (CRYSTAL-FACE) (Jensen et al. 2004), which
102 conducted research flights in the vicinity of sub-tropical and tropical deep convection to study
103 the effects of convectively generated gravity waves (Wang et al. 2006). However, systematic *in-*
104 *situ* measurements of mesoscale gravity waves, especially those associated with upper-
105 tropospheric jet-front systems in the ExUTLS are very scarce. Relevant work includes Nastrom
106 and Fritts (1992) and Fritts and Nastrom (1992), who used commercial aircraft measurements to
107 infer the different sources of gravity waves (convections, front, topography, and jet streaks).
108 They found that mesoscale variances of horizontal wind and temperature were large at the jet-
109 front vicinity regions. However, little is known quantitatively about the generation mechanisms,
110 propagation and characteristics of gravity waves associated with the tropospheric jet streaks.
111 This is due in part to the fact that gravity waves are transient in nature and hard to resolve with
112 regular observing networks (Zhang et al. 2004).

113 The recent Stratosphere-Troposphere Analyses of Regional Transport 2008 (START08)
114 experiment was conducted to examine the chemical structure of the ExUTLS in relation to
115 dynamical processes spanning a range of scales (Pan et al. 2010). In particular, one specific goal

116 of START08 was to observe the properties of gravity waves generated by multiple sources,
117 including jets, fronts, and topography. During the START08 field campaign, a total of 18
118 research flight (RF) missions were carried out during April-June 2008 from the NCAR aviation
119 facility in Broomfield, Colorado (also see the online field catalog of the 18 RFs at
120 http://catalog.eol.ucar.edu/start_08/missions/missions.html). The second flight (RF02), which
121 occurred on 21-22 April 2008, was dedicated, to our knowledge for the first time, to probing
122 mesoscale gravity waves associated with a strong upper-tropospheric jet-front system, even
123 though some previous studies may have recognized the presence of these waves (e.g., Shapiro
124 and Kennedy 1975; Koch et al. 2005). Although only one flight specifically targeted gravity
125 waves, many of the other flights during START08 obtained high-quality observations of gravity
126 waves in the ExUTLS under a wide range of meteorological conditions. This study is an analysis
127 of the gravity wave observations from the START08 mission.

128 A brief description of the experimental design for RF02 and its corresponding
129 meosocscale simulation are presented in section 2, followed in section 3 by a review of the flight-
130 level measurements. Section 4 investigates the localized wave variance with wavelet analysis
131 and examines the polarization relationship based on cospectrum/quadaspectrum analysis.
132 Several examples of wave-like variances are shown and discussed in section 5. Section 6
133 contains a summary.

134

135 **2. Experimental design**

136 The GV research aircraft is ideally suited for investigating gravity waves in the ExUTLS
137 region. The flight ceiling of the aircraft is about 14 km with the START08 payload, which
138 enables sampling the vertical structure of the ExUTLS. With a typical flight speed of ~ 250 m/s at

139 cruise altitude, the flight duration of ~8 hours for a single flight enables the GV to sample a large
140 geographic area with high-resolution (1-Hz) *in-situ* observations. A total of 68 flight segments
141 (color lines in Fig. 1) during the START08 are selected for analysis (also see Fig. 2 in Pan et al.
142 2010 for GV ground tracks of the 18 RFs). Each of these flight segments is longer than 200 km
143 and has near-constant flight-level static pressure and a relatively straight path. This will largely
144 eliminate spurious wave variance due to rapid changes in direction or altitude. In particular, the
145 RF02 mission was conducted over the central United States (38.87-51.10°N, 94.00-109.95°W) to
146 study the gravity wave excitation from a jet-front system and topography in the ExUTLS (Fig. 2
147 and Table 1). It started at 17:53 UTC on 21 April 2008 and finished at 02:54 UTC on 22 April
148 2008. This ~8-hour flight covered a total horizontal distance of ~6700 km, mostly in the lower
149 stratosphere. Five flight segments (thick blue lines in Fig. 1; thick blue lines in Fig. 2b-Fig. 2f;
150 details in section 3) in RF02 are used here. For most of the 5 flight segments, the aircraft flew at
151 an altitude of ~12.5 km (red lines in Fig. 3d; Table 1) and at a speed of ~250 ms⁻¹ (Table 1).

152 The Weather Research and Forecast (WRF) model (Skamarock et al. 2005) was used for
153 flight-planning forecasts. Real-time forecasts used WRF version 2.2.1 and were run with 45-km
154 and 15-km grid spacing for single deterministic forecasts (D1 and D2 in Fig. 1) and 45-km grid
155 spacing for ensemble prediction (D1 only). The model was initialized with a 30-member
156 mesoscale ensemble-based multi-physics data assimilation system (Zhang et al. 2006; Meng and
157 Zhang 2008a,b) and assimilated standard radiosonde observations. The real-time WRF forecasts
158 were archived at the START08 field catalog ([http://catalog.eol.ucar.edu/cgi-](http://catalog.eol.ucar.edu/cgi-bin/start08/model/index)
159 [bin/start08/model/index](http://catalog.eol.ucar.edu/cgi-bin/start08/model/index)). The flight track of RF02 was assigned to fly across the jet exit region
160 and gravity wave active area predicted by the real-time forecasts (also see Fig. 11 in Pan et al.
161 2010 for the real-time mesoscale forecast of gravity waves). Higher-resolution post-mission

162 WRF simulations with 5-km and 1.67-km grid spacing (D3 and D4 in Fig. 1) were also
163 conducted to examine the role of small-scale dynamical processes (e.g., convection and gravity
164 waves), which will be briefly reported in section 3. Nevertheless, an in-depth investigation of the
165 gravity wave dynamics based on the high-resolution post-mission WRF simulations is beyond
166 the scope of the current study, and will be reported elsewhere.

167

168 **3. Overview of the flight-level measurements**

169 Figure 2 depicts the track design of the entire flight and five flight segments during RF02,
170 along with the horizontal wind speed and the smoothed horizontal divergence near the flight
171 level simulated by the high-resolution post-mission WRF simulations valid at different
172 representative times of each five segments. Three flight segments pass mainly along an upper-
173 tropospheric jet streak. These are labeled J1, J2, and J3 and are displayed in Fig. 2b, 2c, and 2d,
174 respectively. Two other flight segments cross the mountains and high plains of Colorado and
175 Kansas. These are labeled M1 and M2 and are displayed in Fig. 2e and 2f, respectively. Flight
176 segment J3 is the longest during RF02. That segment includes flight through or above: the jet
177 core (gray shading in Fig. 2), a jet over high mountains (see the terrain map in Fig. 1), the exit
178 region of the jet, and a surface cold front (not shown). The other two segments, J1 and J2, were
179 intended to be a single segment, but an altitude change was necessary due to air traffic control.

180 Guided by the WRF model forecasts (e.g., Fig. 11 in Pan et al. 2010), this GV flight
181 mission sampled WRF-predicted gravity waves with different potential sources including
182 imbalance of jet streak and orographic forcing. Figure 3 shows the along-track horizontal
183 velocity component (u), across-track horizontal velocity component (v), horizontal wind speed
184 (V ; $V = \sqrt{u^2 + v^2}$), vertical velocity component (w), potential temperature (θ), corrected static

185 pressure (p_c), static pressure (p_s), hydrostatic pressure correction (p_h) derived from the airborne
186 *in-situ* measurements as well as flight height, and terrain along each of the five flight segments.
187 To facilitate spectral and wavelet analyses of these measurements, each variable from the 1-Hz
188 aircraft measurement along the flight segment is linearly interpolated into 250-m spatial series
189 with fixed resolution in distance. The right-hand rule is used to determine the relationships
190 among the positive along-track directions, the positive across-track directions, and the positive
191 vertical directions. For segments J1, J2, and J3, the positive along-track (across-track) directions
192 are all approximately toward the northeast (northwest). For segments M1 and M2, the positive
193 along-track (across-track) directions are both approximately toward the east (north). The
194 corrected static pressure p_c is calculated using the formula of Smith et al. (2008, their equation
195 12):

$$p_c = p_s + p_h = p_s + \bar{\rho}g(z - z_{ref}) \quad (1)$$

196 where z is the GPS altitude, z_{ref} is the average altitude of flight segment and $\bar{\rho}$ is the average
197 density of flight segment. Corrected static pressure p_c from equation 1 is to correct the measured
198 static pressure p_s to a common height level (i.e., z_{ref}) based on the assumption of local
199 hydrostatic balance. Smith et al. (2008) suggests that the contribution of p_s to p_c is much smaller
200 than p_h , because it is assumed that the aircraft almost flies on an isobaric surface.
201

202 Consistent with what was predicted by the real time WRF forecast guidance (as shown in
203 Fig.11 of Pan et al. 2010) as well as simulated by the high-resolution post-mission WRF
204 simulations (in particular the horizontal divergence as potential signals of gravity waves as
205 shown in Fig. 2), the GV *in-situ* measurements of different atmospheric variables suggest there
206 are prevalent gravity wave activities along almost every leg of the 8-hr flight, most notably in the
207 vertical motion field. The largest amplitude of w (over 2 m/s) is during the middle portion of

208 segment J3 (location 680-780 km) on the lee slopes of the Rocky Mountains (also see the
209 discussion in section 5.2). The high terrain and the lee slopes also have the enhanced vertical
210 motions for both segment M1 and segment M2. Though not as large in amplitude, enhanced
211 fluctuations of vertical motions are also observed in the northern end of segment J3, which is in
212 the exit region of the upper-level jet streak and above the surface front. The enhanced variances
213 of vertical motion, accompanied by the changes in horizontal wind and potential temperature,
214 may be associated with topography for both M1 and M2 segments, even though the role of jet
215 cannot be isolated.

216 Power spectra of five selected aircraft measurement variables are given in Fig. 4 for each
217 of the five flight segments during RF02. The calculations of the spectra are performed with the
218 “specx_anal” function in the NCAR Command Language (NCL). Several steps are done before
219 the calculations. Firstly, the mean and least squares linear trend in each of the series are
220 removed. Secondly, smoothing by averaging 7 periodogram estimates is performed. Thirdly,
221 10% of the series are tapered. For segment J1, u , v , θ and p_c have several significant spectral
222 peaks for wavelengths ranging from 16-128 km (mesoscales). The statistically significant
223 spectral peaks in w are more for smaller scales, one at 2-4 km, and the other at 8-32 km. The
224 spectral characteristics for segment J2 are mostly the same as J1 except for much less power at
225 longer wavelengths (16-128 km) and only one peak at smaller scales (2-8 km). For segment J3,
226 both u and θ have statistically significant spectral peaks at mesoscales (\sim 50 and 128 km) and at
227 smaller scales (8-16 km), the later (not the former) of which is also very pronounced for the w
228 spectrum. No significant spectral peak is found for the corrected static pressure p_c for segment
229 J3, except at 512 km, which is likely a reflection of the sub-synoptic scale pressure patterns at
230 the flight level (Fig. 2d). For segment M1, there is a significant mesoscale spectral peak at

231 around 32-64 km for u , θ and p_c , while smaller-scale variations from 4-16 km are also
232 significant for nearly all variables except for p_c . There are almost no significant spectral peaks
233 for all 5 variables for segment M2 except for around 2 km for w .

234 Past studies from both aircraft observations (e.g., Nastrom and Gage 1985; Bacmeister et
235 al. 1996; Lindborg 1999) and numerical simulations (e.g., Skamorcok 2004; Waite and Snyder
236 2013) have revealed/verified the existence of an approximate $-5/3$ power law that is expected for
237 the direct energy cascade in isotropic three-dimensional turbulence (e.g., Kolmogorov 1941) and
238 the inverse cascade in two dimensions (e.g., Kraichnan 1967), as well as an approximate -3
239 power law that is expected for quasigeostrophic turbulence theory (e.g., Charney 1971). The
240 spectral slopes of different variables derived from the flight-level measurements from START08
241 are thus examined here in detail. Overall in segment J3, the spectrum slope for θ (the third
242 column in Fig. 4d) is remarkably similar to those for u (the third column in Fig. 4a) and v (the
243 third column in Fig. 4b), except that there appears to be a deviation from both -3 and $-5/3$ power
244 laws for scales of ~ 8 – ~ 16 km. The spectral slope of w (the third column in Fig. 4c) is also similar
245 to that of θ (the third column in Fig. 4d) for all scales below 32 km, including the above-
246 mentioned deviation. However, for scale larger than ~ 32 km, the slope of w (the third column in
247 Fig. 4c) quickly dropped to almost zero, which is consistent with the continuity equation for
248 near-balanced non-divergent large-scale motions.

249 There are also similarities and differences in spectral slopes among different flight
250 segments depicted in Fig. 4. For example, the above-mentioned spectral shapes of u and v from
251 segment J3 are similar to those from segment J2 (i.e., the second and third columns in Fig. 4a
252 and Fig 4b). Such consistent signals probably result from sampling under similar large-scale
253 background flow at similar flight altitude with almost identical topography, especially between

254 the adjacent flight segments J1+J2 and J3. Despite the overall resemblance among the flight
255 segments of RF02, there are some unique characteristics in the power spectral distributions for
256 individual segments. For segments M1 and M2, for example, (i.e., the fourth column versus the
257 fifth column in Fig. 4), the slopes of u and v during segment M1 are approximately consistent
258 with a -3 power law for the scale of $\sim 0.5\text{--}8$ km, while those during segment M2 follows a $-5/3$
259 power law instead. This is probably associated with the fact that segment M2 successfully
260 captures a rapid decrease in u (from ~ 65 m/s to ~ 40 m/s) while segment M1 has no such a
261 dramatic reduction in u (the fourth column in Fig. 3a versus the fifth column in Fig. 3a). Note
262 that the aircraft during segment M1 flew away from the jet core region, as the jet was still
263 moving eastward to the downhill side of the topography. In contrast, the aircraft during segment
264 M2 flew directly toward the approaching jet core at a lower flight level than segment M1 (the
265 fourth column in Fig. 3d versus the fifth column in Fig. 3d), and the observed decline of u (i.e., a
266 potential jet exit region) is located roughly on the downhill side of the topography (the fifth
267 column in Fig. 3d). This suggests that the spectral slopes for the aircraft measurements can, in
268 fact, be extremely sensitive to changes in the background flow, even though sampling takes place
269 in the same area only a few hours apart.

270 Figure 5 shows composite spectra for eight selected variables averaged over 68 flight
271 segments. Unsurprisingly, the composite spectra are much smoother due to averaging. For u
272 (Fig. 5a), v (Fig. 5b), and horizontal wind speed V (Fig. 5d), the slope of the power spectra are
273 consistent with a $-5/3$ power law for scales above $\sim 8\text{--}16$ km. For w (Fig. 5c), its spectral slope
274 is generally consistent with -3 power laws for the scale of $\sim 0.5\text{--}2$ km but is nearly zero for
275 scales over 32 km, while the slopes in between ($\sim 2\text{--}32$ km) appear to follow an approximate $-$
276 $5/3$ power law, with a statistically significant spectral peak at $\sim 8\text{--}16$ km. Even though the kinetic

277 energy spectra (Fig. 5e) may show a $-5/3$ slope that covers a larger range, the -3 slope over small
278 scale in KE is still evident. For θ (Fig. 5f) at scales between ~ 0.5 km and ~ 2 km, its slope also
279 obeys a -3 power law. For θ (Fig. 5f) at the scale greater than $\sim 8\sim 16$ km, the slope of power
280 spectrum tends to have a $-5/3$ slope, which is similar to u (Fig. 5a), v (Fig. 5b), and V (Fig. 5d)
281 for the same scales. For all the three pressure-related variables (i.e., p_c in Fig. 5g, p_s in Fig. 5h,
282 p_h in Fig. 5i), their slopes generally fall around a $-5/3$ power law, except for scales less than ~ 4
283 km in p_h (Fig. 5i). However, it is noteworthy that there is a sudden concavity (convexity) in p_c
284 (p_s or p_h) for scales between ~ 4 km and ~ 16 km (also see the discussion in section 5.3).

285

286 4. Wavelet analysis

287 4.1 Single-variable wavelet analysis

288 Standard spectral analysis methods characterize the variance as a function of wavelength
289 for an entire data record (flight segment), but do not indicate where variance of a particular
290 wavelength is located within the data record. We use wavelet analysis to complement the
291 spectral analysis in section 3 to study the variance as a function of wavelength within the five
292 flight segments from RF02. A Morlet wavelet function is employed in this study (e.g., Torrence
293 and Compo 1998; Zhang et al. 2001; Woods and Smith 2010). This is a continuous wavelet
294 transform that uses non-orthogonal complex wavelet functions comprising a plane wave
295 modulated by a Gaussian function (e.g., equation 1 in Torrence and Compo 1998):

$$296 \quad \psi_0(\eta) = \pi^{-1/4} e^{i\omega_0\eta} e^{-\eta^2/2} \quad (2)$$

297 where ω_0 is the dimensionless wave number and η is the dimensionless distance. Here ω_0 is set
298 to 6 to satisfy the admissibility condition (Farge 1992). The continuous wavelet transform, used

299 to extract localized spectral information, is defined as the convolution of the series of interest x
300 with the complex conjugate of the wavelet (e.g., equation 2 in Torrence and Compo 1998)

$$301 \quad W_n(s) = \sum_{n'=0}^{N-1} x_{n'} \psi^* \left[\frac{(n'-n)\Delta x}{s} \right] \quad (3)$$

302 where $*$ is the complex conjugate, n is the localized position index, s is the wavelet scale, and
303 Δx is the resolution of the data (0.25 km in this case). The cone of influence (COI) shows the
304 region of the wavelet spectrum where the edge errors cannot be ignored. Computation of the
305 wavelet spectrum and edge error is performed with the wavelet function of equation 3 (Torrence
306 and Compo 1998) in NCL.

307 Figure 6 contains the wavelet power spectra of five selected observed variables along the
308 five selected flight segments of RF02. Using the long segment J3 as an example again (third
309 column in Fig. 6), there is a substantial peak in the power of u (Fig. 6a) at wavelengths around
310 128-km between 400 and 700 km along the flight leg (also seen in p_c of Fig. 6e); ~ 100 -km wave
311 power peaks at location 100-300 km; the wave power of wavelength from ~ 64 km to ~ 128 km
312 also peaks at location 1200-1400 km. The greatest similarity is between the spectra of w and θ
313 (Figs. 6c and d). For example, from location 100 km to 800 km during segment J3, local
314 maximum of power in w (the third column in Fig. 6c) resembles the one in θ (the third column
315 in Fig. 6d). In particular, three distinguished wave modes (~ 64 km, ~ 32 km, and ~ 10 km in
316 along-track wavelength) collocate at location 600-800 km (downstream of a localized hill around
317 600 km in the third column of Fig. 3d). Relatively persistent ~ 10 -km waves in w are shown at
318 location 200-700 km, which corresponds to a similar peak in the spectral analysis of w in the
319 third column of Fig. 4c. Note that such ~ 10 -km waves are also found in other flight segments in
320 RF02 (e.g., location 0-600 km during segment M1, the fourth column in Fig. 6c) and other

321 research flights in START08 (not shown). Interpretations of such small-scale localized wave
 322 variances, as well as mesoscale localized wave variances, are discussed in section 5.

323

324 *4.2 Polarization relationships from cross-wavelet analysis*

325 Following Woods and Smith (2010), the phase relationship between two variables (e.g., u
 326 and v , hereafter in short noted as $(u'v')_p$) can be determined from the cospectrum $(u'v')_c$ and
 327 quadrature spectrum $(u'v')_q$, which are defined as (also see section 6c in Torrence and Compo
 328 1998; equation 8 and appendix A in Woods and Smith 2010):

$$329 \quad (u'v')_c = \text{Re}\{U_n(s_j)V_n^*(s_j)\} \quad (4)$$

$$330 \quad (u'v')_q = \text{Im}\{U_n(s_j)V_n^*(s_j)\} \quad (5)$$

331 where U_n and V_n represent the wavelet transforms of u and v from equation 3, $U_n(s_j)V_n^*(s_j)$ is
 332 the complex-valued cross-wavelet spectrum, while $\text{Re}\{ \}$ and $\text{Im}\{ \}$ represent the real and
 333 imaginary parts of the variables inside the parentheses, respectively. Woods and Smith (2010)
 334 focus on the energy flux by analyzing $(p_c'w')_c$ from equation 4 for vertically propagating waves
 335 and $(p_c'w')_q$ from equation 5 for vertically trapped/ducted waves. In principle, $(p_c'w')_p$ should
 336 be, theoretically speaking, associated with $(u'w')_p$ $((v'w')_p)$ (e.g., Eliassen and Palm 1960;
 337 Lindzen 1990). This is particularly true for stationary mountain waves, which may be present for
 338 RF02 given complex topography during each of the flight segments. However, in practice,
 339 Woods and Smith (2010, their section 7) argued that the perturbation longitudinal velocity was
 340 noisier than pressure in their study. In addition to equation 4 and equation 5, one can also define
 341 the absolute coherence phase angle as $\frac{180}{\pi} \times \arctan\left(\left|\frac{\text{Im}\{U_n(s_j)V_n^*(s_j)\}}{\text{Re}\{U_n(s_j)V_n^*(s_j)\}}\right|\right)$ (also see section 6d in
 342 Torrence and Compo 1998).

343 The phase relations among multiple variables are examined to further explore whether the
344 enhanced variances from the spectral and wavelet analyses are vertically propagating gravity
345 waves. Figure 7 shows three selected examples of cospectrum analysis (i.e., $(u'w')_c$ in Fig. 7a,
346 $(v'w')_c$ in Fig. 7b, $(p_c'w')_c$ in Fig. 7c), one selected example of quadrature spectrum analysis
347 (i.e., $(\theta'w')_q$ in Fig. 7d), and one example of absolute coherence phase angle for $(\theta'w')_p$ (Fig.
348 7e). In the case of a single monochromatic internal gravity wave propagating vertically, for
349 $(u'w')_c$ (Fig. 7a), positive (negative) values indicate upward (downward) flux of along-track
350 momentum. For $(v'w')_c$ (Fig. 7b), positive (negative) values indicate upward (downward) flux
351 of across-track momentum. For $(p_c'w')_c$ (Fig. 7c), positive (negative) values indicate positive
352 (negative) vertical energy transport. For the quadrature spectrum of $(\theta'w')_q$ (Fig. 7d), values
353 should be nonzero while the absolute coherence phase angle of $(\theta'w')_p$ (Fig. 7e) should be close
354 to 90 degree.

355 We again take segment J3 as an example (the third column in Fig. 7): for the small-scale
356 component with along-track wavelength less than 50 km (horizontal solid line), enhanced but
357 incoherent variances are detected for location 100-500 km and for location 600-800 km, with
358 fluctuating positive and negative values for both $(u'w')_c$ (the third column in Fig. 7a) and
359 $(v'w')_c$ (the third column in Fig. 7b). The variations in the signs of vertical transports of
360 horizontal momentum fluxes imply that this flight segment is sampling waves propagating in
361 both forward and backward direction, assuming the vertical energy transports are generally
362 upward. Correspondingly, the absolute coherence phase angle for $(u'v')_p$ (not shown) also
363 alternates frequently between nearly 0 degree and nearly 90 degree. In particular, some of the
364 enhanced variances in the cospectra for along-track wavelengths from ~4 km to ~16 km, though
365 fluctuating in signs, are significant above the 95% confidence level.

366 For the mesoscale component with wavelengths from ~ 50 to ~ 100 km, remarkable
367 localized quadrature variance is found in $(\theta'w')_q$ (the third column in Fig. 7d) for location 500-
368 800 km, consistent with the wavelet analysis of w in the third column of Fig. 6c and θ in the
369 third column of Fig 6d. The absolute coherence phase angle for $(\theta'w')_p$ in Fig. 7e also
370 demonstrate that the cross-wavelet spectrum between θ and w is mostly dominated by their
371 quadrature spectrum (red color shading in Fig. 7e), though there are some exceptions (blue color
372 shading in Fig. 7e).

373 The similarities/discrepancies among different wavelet cospectra and quadrature spectra
374 examined in Fig. 7 demonstrate the difficulties in gravity wave identification and the
375 uncertainties in gravity wave characteristics estimation based solely on aircraft measurements.

376 In addition to cross-wavelet analysis, the signs of the net fluxes (e.g., $\overline{u'w'}$, $\overline{v'w'}$, and
377 $\overline{w'p_c'}$) at each wavelength can also be estimated by the cospectrum analysis based on Fourier
378 transform over the entire segment (not shown). Generally speaking, for the scale below ~ 32 km,
379 both positive values and negative values are important in $\overline{u'w'}$ and $\overline{v'w'}$, while positive $\overline{w'p_c'}$
380 appears to be more continuous than negative $\overline{w'p_c'}$. For the scale above ~ 32 km, negative $\overline{u'w'}$
381 (positive $\overline{w'p_c'}$) appears to be more continuous than positive $\overline{u'w'}$ (negative $\overline{w'p_c'}$), while there
382 is no dominant sign for $\overline{v'w'}$ one way or the other.

383

384 **5. Selected Wave-like Examples: signal of gravity waves or measurement noise?**

385 This section examines several examples of wave-like variations during segment J3 in
386 more detail. Bandpass-filtered values of selected variables are computed by synthesizing the

387 wavelet transform using wavelets with scales between j_1 and j_2 using (e.g., equation 29 in
 388 Torrence and Compo 1998)

$$389 \quad x_n' = \frac{\Delta j \Delta x^{1/2}}{C_\delta \psi_0(0)} \sum_{j=j_1}^{j_2} \frac{Re\{W_n(s_j)\}}{s_j^{1/2}} \quad (6)$$

390 where Δj is the scale resolution and C_δ is a reconstruction factor taken as 0.776 for Morlet
 391 wavelet. The wavelet-based filter in equation 6 has the advantage in removing noise at each
 392 wave number and isolating single events with a broad power spectrum or multiple events with
 393 different wave number (Donoho and Johnstone 1994; Torrence and Compo 1998).

394 Nine pairs of variables, including $(u'w')_p$, $(v'w')_p$, $(u'v')_p$, $(p_c'u')_p$, $(p_c'v')_p$,
 395 $(p_c'w')_p$, $(\theta'w')_p$, $(p_s'w')_p$, and $(p_h'w')_p$, are selected to examine whether the phase
 396 relationship of the variations in the airborne measurements is consistent with the linear theory for
 397 gravity waves. Generally speaking, the phase relation between two variables can be classified
 398 into two major categories: 1) In-phase or out-of-phase relationships, in which one variable leads
 399 or lags the other variable by approximately 0° or 180° ; 2) Quadrature relationships, in which one
 400 variable leads or lags the other by approximately 90° .

401 The phase relationships for linear gravity waves are determined by theory and their
 402 propagation characteristics. Take $(u'w')_p$, $(v'w')_p$, and $(p_c'w')_p$ as examples, if they have an
 403 in- or out-of-phase relationship, the waves are propagating in the vertical direction; if they have a
 404 quadrature relationship, the waves do not propagate vertically and may be trapped or ducted.
 405 Take $(u'v')_p$ as another example, if they have an in- or out-of-phase relationship, the waves may
 406 be internal gravity waves whose intrinsic frequencies are much higher than the Coriolis
 407 frequency; if they have a quadrature relationship, the waves may be inertio-gravity waves with
 408 intrinsic frequencies close to the Coriolis frequency. For vertically propagating linear gravity
 409 waves, $(\theta'w')_p$ should have a quadrature relationship. According to Smith et al. (2008), p_h'

410 should dominate over p_s' , if the aircraft almost flies on a constant pressure surface.
411 Consequently, $(p_h'w')_p$ should be almost identical to $(p_c'w')_p$.

412

413 *5.1 Examples of mesoscale wave variances*

414 Figure 8 demonstrates an example of potential mesoscale gravity waves selected based on
415 the wavelet analysis of u (Fig. 6a), w (Fig. 6c), θ (Fig. 6d), and p_c (Fig. 6e) for location 250-360
416 km in segment J3 (the exit region of northwesterly jet in Fig. 2d). The wave signals are further
417 highlighted by applying a wavelet-based filter (i.e., equation 6) to extract wavelike variations
418 with along-track wavelength between 100 and 120 km. Panels a, b, d, and e show out-of-phase
419 relationships for $(u'w')_p$, $(v'w')_p$, $(p_c'u')_p$, and $(p_c'v')_p$ respectively; while panels c, f, and i
420 show in-phase relationships for $(u'v')_p$, $(p_c'w')_p$, and $(p_h'w')_p$. Panels g and h show
421 quadrature relationships for $(\theta'w')_p$ and $(p_s'w')_p$. The observed phase relations shown in Fig. 8
422 are generally consistent with linear theory for propagating monochromatic gravity waves, as
423 indicated by the cospectrum/quadrature spectrum analysis in Fig. 7. These signals are likely to be
424 internal gravity waves (due to the in-phase relation of $(u'v')_p$ in Fig. 8c) with positive vertical
425 group velocity (due to their positive vertical energy flux, Fig. 8f).

426 In contrast, Figure 9 is an example of wave-like disturbances that lacks a clear,
427 propagating, linear-wave, phase relationship. This example is also selected based on the wavelet
428 analysis of segment J3 for u , v , and p_c (Figs. 6a, b, and e) for along-track wavelength near 128
429 km and location between 560 and 688 km along the segment. This segment lies above the
430 complex topography as depicted in the third column of Fig. 3d. According to Figs. 9a-9e,
431 $(u'w')_p$, $(u'v')_p$, and $(p_c'u')_p$ seem to have out-of-phase relationships, while $(v'w')_p$ and
432 $(p_c'v')_p$ have almost perfect in-phase relationships. These phase relationships appear to be

433 reasonable and generally consistent with the linear theory. The near in-phase relationship
434 exhibited by $(\theta'w')_p$ (Fig. 9g), however, raises doubts about whether these variations are true
435 gravity waves, as this is not consistent with linear theory. If they are in fact gravity wave signals,
436 the discrepancy highlights the difficulties of extracting gravity wave perturbations from
437 observations. For example, the mesoscale variances may be contaminated by small-scale
438 variability of θ and w due to the coexistence of wave variances at different scales for this region
439 (see the wavelet analysis of w in Fig. 6c in and θ in Fig. 6d). Additionally, there are uncertainties
440 in extracting mesoscale gravity waves from a varying background flow (e.g., Zhang et al. 2004),
441 especially for u , v and θ . Note that θ and w have a very consistent quadrature relation from ~ 8
442 km to ~ 64 km for this region in their quadrature spectrum of Fig. 7d (also see Fig. 7e), but this
443 quadrature relation (the third column in Fig. 7d), including their corresponding wavelet spectrum
444 (the third column in Fig. 6c and Fig. 6d) is much weaker for wavelengths near 128 km for
445 location 560-688 km in segment J3.

446 Consistent with Smith et al. (2008), the amplitude of p_h' is much larger than the
447 amplitude of p_s' for both examples of mesoscale wave variances. Therefore, $(p_h'w')_p$ is almost
448 identical to $(p_c'w')_p$ for both cases (Fig. 8f versus Fig. 8i; Fig. 9f versus Fig. 9i). It appears that
449 the assumption of constant p_s flight height is valid for these two mesoscale examples.

450

451 *5.2 Examples of small-scale wavelike variations*

452 Figure 10 shows an example of short-scale wave-like disturbances that have a phase
453 relationship consistent with linear gravity wave theory based on the wavelet analysis in Fig. 6
454 with scales from 32 to 64 km located at 650 to 750 km during segment J3. In-phase relationships
455 are seen in the filtered signals of $(p_c'v')_p$ (Fig. 10e), while out-of-phase relationships are seen in

456 $(u'v')_p$ and $(p_c'u')_p$ (Figs. 10c and d). Quadrature relationships can generally be seen in
457 $(u'w')_p$, $(v'w')_p$, $(p_c'w')_p$, and $(\theta'w')_p$ (Figs. 10a, b, f, and g). These small-scale waves have
458 no apparent vertical flux of horizontal momentum (Figs. 10a and b) and no vertical energy flux
459 (Fig. 10f), a key sign of vertically trapped gravity waves. Short-scale waves based on GV aircraft
460 measurements and/or numerical simulations are also discussed in Smith et al. (2008), Woods and
461 Smith (2010; 2011).

462 However, parts of the small-scale wave variations derived from the *in-situ* measurements,
463 especially for wavelengths from 5 to 15 km, may be difficult to classify as gravity waves. Figure
464 11 shows an example of short-scale wave variations in the aircraft measurements with along-
465 track wavelengths from 8 to 16 km for locations 680 to 780 km along segment J3. As depicted in
466 Fig. 11, $(u'w')_p$ (Fig. 11a) appears to have a quadrature relationship, even though this relative
467 phase varies, especially for locations from 710 to 730 km. Compared to $(u'w')_p$ (Fig. 11a),
468 $(v'w')_p$ and $(\theta'w')_p$ (Fig. 11b and g) have consistent quadrature relationships within this 100-
469 km distance. On the other hand, $(u'v')_p$ (Fig. 11c) varies significantly from one wavelength to
470 the next. The amplitude of w' in this example is extremely large (~ 2.5 m/s at its maximum) in
471 this selected example. In comparison, the amplitude of p_c' is rather small, and it is actually too
472 small to be noticed when using a wider bandpass window (not shown). Also, the quadrature
473 relationship in $(p_c'w')_p$ (Fig. 11f) is not as remarkable as those in $(u'w')_p$ and $(v'w')_p$ (Figs.
474 11a and b), which appears to contradict the theoretical description of Eliassen and Palm (1960)
475 on energy and momentum fluxes (also see Lindzen 1990). In addition, it is worth mentioning that
476 $(p_s'w')_p$ and $(p_h'w')_p$ in Figs. 11h and i have almost perfect out-of-phase and in-phase
477 relationships, respectively.

478 In contradiction to Smith et al. (2008), the amplitude of p_h' in the above example of Fig.
 479 11 is comparable with the amplitude of p_s' (Fig. 11h versus Fig. 11i). Surprisingly, $(p_c'w')_p$,
 480 $(p_s'w')_p$, and $(p_h'w')_p$ are also very different from each other (compare Figs. 11f, h, and i). The
 481 signals of p_s' and p_h' (Fig. 11h and i) are out-of-phase for wavelengths near 10 km and have
 482 comparable amplitude, which leads to nearly no such wave variances in p_c' (Fig. 11d-11f) given
 483 p_c' is the sum of p_s' and p_h' .

484

485 *5.3 Insight from spectral analysis of different pressure variables*

486 Figure 12a compares the power spectrum of three pressure-related variables (i.e.,
 487 corrected static pressure p_c , static pressure p_s , hydrostatic pressure correction p_h ; also see
 488 equation 1). Using segment J3 as an example, for wavelengths greater than ~ 32 km, p_c is almost
 489 identical to p_h ; for wavelengths between ~ 32 km and ~ 4 km, the variances between p_s and p_h
 490 are comparable, and the variances of p_c are noticeably smaller than those in p_s and p_h ; for
 491 wavelengths less than ~ 4 km, p_c is almost identical to p_s . Figure 12b shows the quantity

492 $\sqrt{\frac{spec(p_s)+spec(p_h)}{spec(p_c)}}$, where $spec()$ indicates the power spectrum of the variable inside the

493 parentheses (e.g., Figs. 4-5). For segment J3, the square root of the ratio is close to 1.0 for the
 494 wavelengths greater than ~ 32 km and less than ~ 4 km. At intermediate wavelengths, the square
 495 root of the ratio reaches a maximum near 10 for wavelengths of ~ 10 km. This suggests that p_s'
 496 and p_h' may tend to cancel each other at intermediate scales, which reduces the amplitude of p_c'
 497 at these intermediate wavelengths (also see the example in Fig. 11) since p_c' is the sum of p_s'
 498 and p_h' . Similar behaviors can be also observed in other segments, although the exact ranges of
 499 the intermediate wavelengths may be different from case to case.

500 Figure 12 suggests that the assumption of constant p_s flight height may not be valid at all
501 scales, though it appears to be true for mesoscale waves. In consequence, p_h' may not always
502 dominate over p_s' as assumed in Smith et al. (2008). The spectral analysis and wavelet analysis
503 of p_s (not shown) demonstrate that p_s indeed has relatively large variances for the short-scale
504 range, and that p_s and w share some common characteristics (also see Fig. 3). Moreover, the
505 hydrostatic approximation, which is the underlying assumption for equation 1, may no longer be
506 valid for short scales.

507

508 **6. Concluding remarks and discussion**

509 One of the primary objectives of the recent START08 field experiment is to characterize
510 the sources and impacts of mesoscale waves with high-resolution flight-level aircraft
511 measurements and mesoscale models. The current study focuses on the second research flight
512 (RF02), which was the first airborne mission dedicated to probing gravity waves associated with
513 strong upper-tropospheric jet-front systems and high topography. Based on spectral and wavelet
514 analyses of the *in-situ* observations, along with a diagnosis of the polarization relationships, it is
515 found that there are clear signals of significant mesoscale variations with wavelengths ranging
516 from ~50 to ~500 km in almost every segment of the 8-hr flight (order ranging from 0.01 m/s to
517 1.0 m/s in vertical motion), which took place mostly in the lower stratosphere. The flow sampled
518 by the aircraft covers a wide range of background conditions including near the jet core, a jet
519 over the high mountains, and the exit region of the jet. There is clear evidence of vertically
520 propagating gravity waves of along-track wavelengths between 100 and 120 km during some of
521 the flight segments. There are also some indications of potential vertically trapped gravity waves
522 of along-track wavelengths between 32 and 64 km.

523 A general summary of power spectra is as follows: (1) Horizontal velocity components
524 and potential temperature for the scale approximately between ~ 8 km and ~ 256 km display the
525 approximate $-5/3$ power law. The common characteristics and individual features of the wave
526 variances and spectrum slope behaviors appear to be generally consistent with past studies on the
527 spectral analysis of aircraft measurements, including Nastrom and Gage (1985) using the Global
528 Atmospheric Sampling Program (GASP) flight dataset, and Lindborg (1999) using the
529 Measurement of Ozone and Water Vapor by Airbus In-Service Aircraft (MOZAIC) aircraft
530 observations. In addition, our recent separate study of idealized moist baroclinic waves (Sun and
531 Zhang 2015) suggests that the presence of moist convection and mesoscale gravity waves,
532 though probably non-isotropic, does appear to steer the mesoscale range of the spectral slope to
533 be $-5/3$. (2) Vertical velocity component appears to be flat approximately within the range
534 between ~ 8 km and ~ 256 km. (3) The power spectra of horizontal velocity components and
535 potential temperature roll over to a -3 power law for the scale between ~ 0.5 km and ~ 8 km.
536 Based on three aircraft campaign projects, Bacmeister et al. (1996) has also reported the small-
537 scale steepening behavior. The characteristics in (3) are generally observed except (4) when this
538 part of the spectrum is activated, as recorded clearly by M2, one of the highlighted flight
539 segments. Interestingly, the M1 segment immediately prior to the M2 segment did not record the
540 event, probably due to the fast changing background flow. Spectral behaviors of atmospheric
541 variables have also been studied by high-resolution non-hydrostatic mesoscale numerical
542 weather prediction (NWP) models (e.g., Skamarock 2004; Tan et al. 2004; Zhang et al. 2007;
543 Waite and Snyder 2013; Bei and Zhang 2014).

544 Smaller-scale wavelike oscillations below 50 km are found to be quite transient. In
545 particular, aircraft measurements of several flight segments are dominated by signals with

546 sampled periods of ~20~60 seconds and wavelengths of ~5~15 km (assuming that the typical
547 flight speed is approximately 250 m/s). This study suggests that at least part of the nearly-
548 periodic high-frequency signals might be unphysical and a result of intrinsic observational errors
549 in the aircraft measurements or small-scale flight-altitude fluctuations that are difficult to account
550 for. Such potentially contaminated variations are often collocated with larger-scale wave signals,
551 which in turn may lead to larger uncertainties in the estimation of the wave characteristics. Part
552 of the uncertainties may come from the inability of the aircraft to maintain constant static
553 pressure altitude in the presence of small-scale turbulence. The current study mainly focuses on
554 examining the fluctuations with the use of linear theory for monochromatic gravity waves.
555 Therefore, in addition to measurement errors, the possibilities that those fluctuations may be due
556 to other physical phenomena (e.g., nonlinear dynamics, shear instability and/or turbulence)
557 cannot be completely ruled out in the current study.

558 Although the real-time mesoscale analysis and prediction system gave a reasonable
559 forecast guidance on the region of potential gravity wave activities, it remains to be explored (1)
560 how well the current generation of numerical weather models predicts the excitation of gravity
561 waves, (2) how often gravity waves break in the ExUTLS region, and (3) what evidence in tracer
562 measurements is shown for the contribution of gravity wave breaking to mixing. Future work
563 will also seek to examine the origin and dynamics of the gravity waves observed during RF02 of
564 START08 through a combination of observations and numerical modeling. This will help to
565 distinguish whether the sampled mesoscale and small-scale variances are gravity waves or
566 artifacts of the observing system. In addition, under the idealized controllable atmosphere with
567 varying degrees of convective instability and baroclinic instability (e.g., Zhang 2004; Wang and
568 Zhang 2007; Wei and Zhang 2014; Sun and Zhang 2015), high-resolution simulations of

569 baroclinic jet/front systems will be employed to understand (1) how to constrain the
570 parameterizations of jet/front gravity waves in general circulation models, (2) the role of gravity
571 waves in mesoscale predictability, and (3) the contribution of gravity waves to mesoscale energy
572 spectra in global wavenumber distribution or in multi-dimensional wavenumber distribution.

573

574 **Acknowledgments:** The START08 experiment is sponsored by the National Science Foundation
575 (NSF). A large number of people contributed to the success of START08 experiment. The
576 dedication of the instrument team, co-sponsored by NCAR, University of Colorado, Harvard
577 University, University of Miami, Princeton University, NOAA Earth System Research
578 Laboratory (ESRL) Global Monitoring Division (GMD) and Chemical Science Division (CSD),
579 and the NCAR Research Aviation Facility staff in running the flight operation are the key factors
580 in the success of campaign. We also acknowledge the effort and skill of the GV pilots Henry
581 Boynton and Ed Ringleman, which was critical to meeting mission objectives. We benefit from
582 review comments from the editor Tim Dunkerton and four anonymous reviewers on an earlier
583 versions of the manuscript. This research is sponsored by NSF grants 0618662, 0722225,
584 0904635, and 1114849. Computing is performed at the Texas Advanced Computing Center
585 (TACC).

586 **References**

- 587 Alexander, M. J., and K. H. Rosenlof, 2003: Gravity-wave forcing in the stratosphere:
588 Observational constraints from the Upper Atmosphere Research Satellite and implications for
589 parameterization in global models. *J. Geophys. Res. – Atmos.*, 108: Art. No. 4597.
- 590 Bacmeister, J. T., S. D. Eckermann, P. A. Newman, L. Lait, K. R. Chan, M. Loewenstein, M. H.
591 Proffitt, and B. L. Gary, 1996: Stratospheric horizontal wavenumber spectra of winds, po-
592 tential temperature, and atmospheric tracers observed by high-altitude aircraft. *J. Geophys.*
593 *Res.*, 101, 9441–9470.
- 594 Bei, N., and F. Zhang, 2014: Mesoscale Predictability of Moist Baroclinic Waves: Variable and
595 Scale Dependent Error Growth. *Advances in Atmospheric Sciences*, doi: 10.1007/s00376-
596 014-3191-7.
- 597 Bertin F., Campistron B., Caccia J. L., Wilson R., 2001: Mixing processes in a tropopause
598 folding observed by a network of ST radar and lidar. *Annales Geophysicae*, 19, 953-963.
- 599 Bosart, L. F., W. E. Bracken, and A. Seimon, 1998: A study of cyclone mesoscale structure with
600 emphasis on a large-amplitude inertia-gravity waves. *Mon. Wea. Rev.*, 126, 1497-1527.
- 601 Brown, P. R. A., 1983: Aircraft measurements of mountain waves and their associated
602 momentum flux over the british isles. *Q. J. R. Meteorol. Soc.*, 109, 849-865.
- 603 Charney, J. G., 1971: Geostrophic turbulence. *J. Atmos. Sci.*, 28, 1087–1095.
- 604 Donoho, D. L., and I. M. Johnstone, 1994: Ideal spatial adaptation by wavelet shrinkage.
605 *Biometrika*, 81, 425–455.
- 606 Dornbrack, A., T. Birner, A. Fix, H. Flentje, A. Meister, H. Schmid, E. V. Browell, and M.
607 J. Mahoney, 2002: Evidence for inertia gravity waves forming polar stratospheric clouds
608 over scandinavia. *J. Geophys. Res.*, 107, 8287, doi:10.1029/2001JD000452.

609 Doyle, J., H. Volkert, A. Dornbrack, K. Hoinka, and T. Hogan, 2002: Aircraft measurements and
610 numerical simulations of mountain waves over the central Alps: A pre-MAP test case. *Q. J.*
611 *R. Meteorol. Soc.*, 128, 2175-2184.

612 Einaudi, F., A. J. Bedard, and J. J. Finnigan, 1989: A climatology of gravity waves and other
613 coherent disturbances at the Boulder Atmospheric Observatory during March–April 1984. *J.*
614 *Atmos. Sci.*, 46, 303–329.

615 Eliassen, A. and E. Palm, 1960: On the transfer of energy in stationary mountain waves. *Geophys.*
616 *Publ.*, 22, 1-23.

617 Farge, M., 1992: Wavelet transforms and their applications to turbulence. *Annu. Rev. Fluid*
618 *Mech.*, 24, 395-457.

619 Fritts, D. C., and G. D. Nastrom, 1992: Sources of mesoscale variability of gravity waves. Part
620 II: Frontal, convective, and jet stream excitation. *J. Atmos. Sci.*, 49, 111-127.

621 Gong, J., and M. A. Geller, 2010: Vertical fluctuation energy in United States high vertical
622 resolution radiosonde data as an indicator of convective gravity wave sources. *J. Geophys.*
623 *Res.* 115 (D11): 10.1029/2009JD012265.

624 Grivet-Talocia, S., F. Einaudi, W. L. Clark, R. D. Dennett, G. D. Nastrom, and T. E. VanZandt,
625 1999: A 4-yr Climatology of Pressure Disturbances Using a Barometer Network in Central
626 Illinois. *Mon. Wea. Rev.*, 127, 1613–1629.

627 Grubišić, V., J.D. Doyle, J. Kuettner, S. Mobbs, R.B. Smith, C.D. Whiteman, R. Dirks, S.
628 Czyzyk, S.A. Cohn, S. Vosper, M. Weissmann, S. Haimov, S.F.J. De Wekker, L.L. Pan, and
629 F.K. Chow, 2008: The Terrain-Induced Rotor Experiment. *Bull. Amer. Meteor. Soc.*, 89,
630 1513–1533.

631 Hertzog, A., and F. Vial, 2001: A study of the dynamics of the equatorial lower stratosphere by
632 use of ultra-long-duration balloons: 2. Gravity waves. *J. Geophys. Res.*, 106, 22 745– 22 761.

633 Jensen, E. J., D. Starr, and O. B. Toon, 2004: Mission investigates tropical cirrus clouds. *EOS*,
634 85, 45-50.

635 Kaplan, M. L., S. E. Koch, Y.-L. Lin, R. P. Weglarz, and R. A. Rozumalski, 1997: Numerical
636 simulations of a gravity wave event over CCOPE. Part I: The role of geostrophic adjustment
637 in mesoscale jetlet formation. *Mon. Wea. Rev.*, 125, 1185–1211.

638 Karacostas, T. S. and J. D. Marwitz, 1980: Turbulent kinetic energy budgets over
639 mountainousterrain. *J. Appl. Meteor.*, 19, 163-174.

640 Koch S.E., Jamison B.D., Lu C.G., Smith T.L., Tollerud E.I., Girz C., Wang N., Lane T.P.,
641 Shapiro M.A., Parrish D.D., Cooper O.R., 2005: Turbulence and gravity waves within an
642 upper-level front, *J. Atmos. Sci.*, 62, 3885-3908.

643 Koch, S. E., F. Zhang, M. Kaplan, Y.-L. Lin, R. Weglarz, and M. Trexler, 2001: Numerical
644 simulation of a gravity wave event observed during ccope. part 3: the role of a mountain-
645 plains solenoid in the generation of the second wave episode. *Mon. Wea. Rev.*, 129, 909–
646 932.

647 Kolmogorov, A. N., 1941: The local structure of turbulence in incompressible viscous fluid for
648 very large Reynolds number. *Dokl. Akad. Nauk SSSR*, 30, 301–305.

649 Koppel, L. L., L. F. Bosart, and D. Keyser, 2000: A 25-yr climatology of large-amplitude hourly
650 surface pressure changes over the conterminous United States. *Mon. Wea. Rev.*, 96, 51–68.

651 Kraichnan, R. H., 1967: Inertial ranges in two-dimensional turbulence. *Phys. Fluids*, 10, 1417–
652 1423.

653 Lane, T. P., J. D. Doyle, R. Plougonven, M. A. Shapiro, and R. D. Sharman, 2004: Ob-
654 servations and numerical simulations of inertia-gravity waves and shearing instabilities in the
655 vicinity of a jet stream. *J. Atmos. Sci.*, 61, 2692–2706.

656 Lane, T. P., M. J. Reeder, T. L. Clark, 2001: Numerical Modeling of Gravity Wave Generation
657 by Deep Tropical Convection. *J. Atmos. Sci.*, 58, 1249–1274.

658 Laursen, K. K., D. P. Jorgensen, G. P. Brasseur, S. L. Ustin, and J. R. Huning, 2006: HIAPER:
659 The next generation NSF/NCAR research aircraft. *Bull. Amer. Meteor. Soc.*, 87, 896-909.

660 Leutbecher, M. and H. Volkert, 2000: The propagation of mountain waves into the stratosphere:
661 Quantitative evaluation of three-dimensional simulations. *J. Atmos. Sci.*, 57, 3090-3108.

662 Lilly, D. K. and P. J. Kennedy, 1973: Observations of a stationary mountain wave and its
663 associated momentum flux and energy dissipation. *J. Atmos. Sci.*, 30, 1135-1152.

664 Lin, Y., and F. Zhang, 2008: Tracking gravity waves in baroclinic jet-front systems. *J. Atmos.*
665 *Sci.*, 65, 2402-2415.

666 Lindborg, E., 1999: Can the atmospheric kinetic energy spectrum be explained by two-
667 dimensional turbulence? *J. Fluid Mech.*, 388, 259 –288.

668 Lindzen, R. S., 1990: *Dynamics in Atmospheric Physics*. Cambridge University Press, 320 pp.

669 Meng, Z, and F. Zhang, 2008a: Test of an ensemble-Kalman filter for mesoscale and regional-
670 scale data assimilation. Part III: Comparison with 3Dvar in a real-data case study. *Mon. Wea.*
671 *Rev.*, 136, 522-540.

672 Meng, Z, and F. Zhang, 2008b: Test of an ensemble-Kalman filter for mesoscale and regional-
673 scale data assimilation. Part IV: Performance over a warm-season month of June 2003. *Mon.*
674 *Wea. Rev.*, 136, 3671-3682.

675 Mirzaei, M., C. Zülicke, A. Mohebalhojeh, F. Ahmadi-Givi, and R. Plougonven (2014),
676 Structure, energy, and parameterization of inertia-gravity waves in dry and moist simulations
677 of a baroclinic wave life cycle, *J. Atmos. Sci.*, 71, 2390–2414. doi:
678 <http://dx.doi.org/10.1175/JAS-D-13-075.1>

679 Moustou, M., H. Teitelbaum, P. F. J. van Velthoven, and H. Kelder, 1999: Analysis of gravity
680 waves during the POLINAT experiment and some consequences for stratosphere-troposphere
681 exchange. *J. Atmos. Sci.*, 56, 1019-1030.

682 Nastrom, G. D., and D. C. Fritts, 1992: Sources of mesoscale variability of gravity waves. Part I:
683 Topographic excitation. *J. Atmos. Sci.*, 49, 101–110.

684 Nastrom, G. D., and K. S. Gage, 1985: A Climatology of Atmospheric Wavenumber Spectra of
685 Wind and Temperature Observed by Commercial Aircraft. *J. Atmos. Sci.*, 42, 950–960.

686 O’Sullivan, D. and T. J. Dunkerton, 1995: Generation of inertia-gravity waves in a simulated life
687 cycle of baroclinic instability. *J. Atmos. Sci.*, 52, 3695–3716.

688 Pan, L. L., K. P. Bowman, E. L. Atlas, S. C. Wofsy, F. Zhang, and co-authors, 2010:
689 Stratosphere-Troposphere Analyses of Regional Transport Experiment. *Bulletin of the*
690 *American Meteorological Society*, 91, 327-342.

691 Pavelin E., J.A. Whiteway, G. Vaughan, 2001: Observation of gravity wave generation and
692 breaking in the lowermost stratosphere. *J. Geophys. Res.*, 106 (D6), 5173-5179.

693 Plougonven, R. and C. Snyder, 2007: Inertia-gravity waves spontaneously generated by jets and
694 fronts. Part I: Different baroclinic life cycles. *J. Atmos. Sci.*, 64, 2502–2520.

695 Plougonven, R., and F. Zhang, 2014: Internal gravity waves from atmospheric jets and fronts.
696 *Reviews of Geophysics*, 52, doi: 10.1002/2012RG000419.

697 Plougonven, R., H. Teitelbaum, and V. Zeitlin, 2003: Inertia gravity wave generation by
698 tropospheric midlatitude jet as given by the fronts and atlantic storm-track experiment radio
699 soundings. *J. Geophys. Res.-Atmos.*, 108, 888–889.

700 Pokrandt, P. J., G. J. Tripoli, and D. D. Houghton, 1996: Processes leading to the formation of
701 mesoscale waves in the midwest cyclone of 15 december 1987. *Mon. Wea. Rev.*, 124, 2726–
702 2752.

703 Poulos, G. S., William Blumen, David C. Fritts, Julie K. Lundquist, Jielun Sun, Sean P. Burns,
704 Carmen Nappo, Robert Banta, Rob Newsom, Joan Cuxart, Enric Terradellas, Ben Balsley,
705 and Michael Jensen, 2002: CASES-99: A Comprehensive Investigation of the Stable
706 Nocturnal Boundary Layer. *Bull. Amer. Meteor. Soc.*, 83, 555–581.

707 Powers, J. G. and R. J. Reed, 1993: Numerical model simulation of the large-amplitude
708 mesoscale gravity-wave event of 15 December 1987 in the central United States. *Mon. Wea.*
709 *Rev.*, 121, 2285–2308.

710 Radok, U., 1954: A procedure for studying mountain effects at low levels. *Bull. Amer. Meteor.*
711 *Soc.*, 35/9, 412.

712 Ramamurthy, M. K., R. M. Rauber, B. Collins, and N. K. Malhotra, 1993: A comparative study
713 of large-amplitude gravity-wave events. *Mon. Wea. Rev.*, 121, 2951–2974.

714 Rauber, R. M., M. Yang, M. K. Ramamurthy, and B. F. Jewett, 2001: Origin, evolution, and
715 fine-scale structure of the St. Valentine’s Day mesoscale gravity wave observed during
716 storm-fest. Part I: Origin and evolution. *Mon. Wea. Rev.*, 129, 198–217.

717 Reeder, M. J., and M. Griffiths, 1996: Stratospheric inertia-gravity waves generated in a
718 numerical model of frontogenesis. II: Wave sources, generation mechanisms and momentum
719 fluxes. *Quart. J. Roy. Meteor. Soc.*, 122, 1175–1195.

720 Schneider, R. S., 1990: Large-amplitude mesoscale wave disturbances within the intense
721 midwest extratropical cyclone of 15 December 1987. *Wea. Forecasting*, 5, 533–558.

722 Shapiro, M. A., and P. J. Kennedy, 1975: Aircraft Measurements of Wave Motions within
723 Frontal Zone Systems. *Mon. Wea. Rev.*, 103, 1050–1054. doi:
724 [http://dx.doi.org/10.1175/1520-0493\(1975\)103<1050:AMOWMW>2.0.CO;2](http://dx.doi.org/10.1175/1520-0493(1975)103<1050:AMOWMW>2.0.CO;2)

725 Skamarock, W. C., 2004: Evaluating Mesoscale NWP Models Using Kinetic Energy Spectra.
726 *Mon. Wea. Rev.*, 132, 3019–3032.

727 Skamarock, W. C., J. B. Klemp, J. Dudhia, D.O. Gill, D. M. Barker, W. Wang, and J. G. Powers,
728 2005: A description of the Advanced Research WRF Version 2. NCAR technical note
729 468+STR, 88 pp.

730 Smith, R. B., 1976: The generation of lee waves by the blue ridge. *J. Atmos. Sci.*, 33, 507-519.

731 Smith, R. B., 1980: Linear theory of stratified hydrostatic flow past an isolated mountain. *Tellus*,
732 348-364.

733 Smith, R. B., B. K. Woods, J. Jensen, W. A. Cooper, J. D. Doyle, Q. Jiang, and V. Grubisic,
734 2008: Mountain waves entering the stratosphere. *J. Atmos. Sci.*, 65, 2543 –2562.

735 Sun, Y. Q., and F. Zhang, 2015: Intrinsic versus practical limits of atmospheric predictability and
736 the significance of the butterfly effect. *J. Atmos. Sci.*, in review.

737 Tan, Z. M., F. Zhang, R. Rotunno, and C. Snyder, 2004: Mesoscale predictability of moist
738 baroclinic waves: Experiments with parameterized convection. *J. Atmos. Sci.*, 61, 1794-
739 1804.

740 Torrence, C., and G. P. Compo, 1998: A practical guide to wavelet analysis. *Bull. Amer. Meteor.*
741 *Soc.*, 19, 61 –78.

742 Uccellini, L. W. and S. E. Koch, 1987: The synoptic setting and possible source mechanisms for
743 mesoscale gravity wave events. *Mon. Wea. Rev.*, 115, 721–729.

744 Vaughan G, Worthington RM, 2000: Break-up of a stratospheric streamer observed by MST
745 radar. *Quarterly Journal of the Royal Meteorological Society*, 126, 1751-1769.

746 Vaughan, G., and R. Worthington, 2007: Inertia-gravity waves observed by the UK MST radar,
747 *Q. J. R. Meteorol. Soc.*, 133(S2), 179–188.

748 Vergeiner, I., and D. K. Lilly, 1970: The dynamic structure of lee wave flow as obtained from
749 balloon and airplane observations. *Mon. Wea. Rev.*, 98, 220-232.

750 Vincent, R. A., and M. J. Alexander, 2000: Gravity waves in the tropical lower stratosphere: An
751 observational study of seasonal and interannual variability. *J. Geophys. Res.*, 105, 17, 971-
752 17, 982.

753 Waite, M. L., and Chris Snyder, 2013: Mesoscale Energy Spectra of Moist Baroclinic Waves. *J.*
754 *Atmos. Sci.*, 70, 1242–1256.

755 Wang, L. and M. J. Alexander, T. P. Bui, and M. J. Mahoney, 2006: Small-scale gravity waves
756 in ER-2 MMS/MTP wind and temperature measurements during CRYSTAL-FACE. *Atmos.*
757 *Chem. Phys.*, 6, 1091-1104.

758 Wang, L., and M. A. Geller, 2003: Morphology of gravity-wave energy as observed from 4 years
759 (1998-2001) of high vertical resolution U.S. radiosonde data, *J. Geophys. Res.*, 108 (D16),
760 4489, doi:10.1029/2002JD002786.

761 Wang, S. and F. Zhang, 2007: Sensitivity of mesoscale gravity waves to the baroclinicity of jet-
762 front systems. *Mon. Wea. Rev.*, 135, 670-688.

763 Wei, J., and F. Zhang, 2014: Mesoscale gravity waves in moist baroclinic jet–front systems. *J.*
764 *Atmos. Sci.*, 71, 929–952. doi: <http://dx.doi.org/10.1175/JAS-D-13-0171.1>

765 Wei, J., and F. Zhang, 2015: Tracking gravity waves in moist baroclinic jet-front systems.
766 Journal of Advanced Modeling in Earth Sciences (JAMES), DOI: 10.1002/2014MS000395

767 Woods, B. K. and R. B. Smith, 2010: Energy flux and wavelet diagnostics of secondary
768 mountain waves. *J. Atmos. Sci.*, 67, 3721-3738.

769 Woods, B. K. and R. B. Smith, 2011: Short-Wave Signatures of Stratospheric Mountain Wave
770 Breaking. *J. Atmos. Sci.*, 68, 635-656.

771 Wu, D. L., and F. Zhang, 2004: A study of mesoscale gravity waves over North Atlantic with
772 satellite observations and a mesoscale model. *J. Geophys. Res.-Atmos.*, 109, D22104.

773 Yamanaka, M. D., S. Ogino, S. Kondo, T. Shimomai, S. Fukao, Y. Shibagaki, Y. Maekawa, and
774 I. Takayabu, 1996: Inertio-gravity waves and subtropical multiple tropopauses: vertical
775 wavenumber spectra of wind and temperature observed by the MU radar, radiosondes and
776 operational rawinsonde network. *J. Atmos. Terr. Phys.*, 58, 785-805.

777 Zhang, F., 2004: Generation of mesoscale gravity waves in the upper-tropospheric jet-front
778 systems. *J. Atmos. Sci.*, 61, 440-457.

779 Zhang, F., and S. E. Koch, 2000: Numerical simulation of a gravity wave event over CCOPE.
780 Part II: Wave generated by an orographic density current. *Mon. Wea. Rev.*, 128, 2777– 2796.

781 Zhang, F., M. Zhang, J. Wei, and S. Wang, 2013: Month-Long Simulations of Gravity Waves
782 over North America and North Atlantic in Comparison with Satellite Observations. *Acta*
783 *Meteorologica Sinica*, 27, 446-454.

784 Zhang, F., N. Bei, R. Rotunno, C. Snyder, and C. C. Epifanio, 2007: Mesoscale predictability of
785 moist baroclinic waves: Convection-permitting experiments and multistage error growth
786 dynamics. *J. Atmos. Sci.*, 64, 3579-3594.

787 Zhang, F., S. E. Koch, and M. L. Kaplan, 2003: Numerical simulations of a large-amplitude
788 gravity wave event. *Meteorology and Atmospheric Physics*, 84, 199–216.

789 Zhang, F., S. E. Koch, C. A. Davis, and M. L. Kaplan, 2001: Wavelet analysis and the governing
790 dynamics of a large-amplitude gravity wave event along the east coast of the United States.
791 *Q. J. R. Meteorol. Soc.*, 127, 2209-2245.

792 Zhang, F., S. Wang, and R. Plougonven, 2004: Uncertainties in using the hodograph method to
793 retrieve gravity wave characteristics from individual soundings. *Geophysical Research*
794 *Letters*, 31, L11110, doi:10.1029/2004GL019841.

795 Zhang, F., Z. Meng, and A. Aksoy, 2006: Tests of an ensemble Kalman filter for mesoscale and
796 regional-scale data assimilation. Part I: Perfect model experiments. *Mon. Wea. Rev.*, 134,
797 722-736.

798 Zhang, S. D., and F. Yi, 2007: Latitudinal and seasonal variations of inertial gravity wave
799 activity in the lower atmosphere over central China, *J. Geophys. Res.*, 112, D05109,
800 doi:10.1029/2006JD007487.

801

802

803 **Figure Captions**

804 **Figure 1.** The 68 Gulfstream V (GV) flight segments (colored lines) selected for wave analysis
805 during START08. The 18 colors represent 18 research flight (RF) missions. The thick blue lines
806 represent the second flight (RF02). The grey shadings give the terrain elevation map (shaded
807 every 250 m) over north America. The 4 black boxes are the model domain design for the second
808 research flight (RF02) during 21-22 April 2008, which are named D1-D4 from coarse to fine
809 domain with horizontal resolution as 45 km, 15 km, 5 km and 1.67 km, respectively. The field
810 catalog of the 18 RFs are available online (at
811 http://catalog.eol.ucar.edu/start_08/missions/missions.html). The GV ground tracks of the
812 18 RFs are also documented in Fig. 2 of Pan et al. (2010).

813

814 **Figure 2.** Simulated pressure at 9 km altitude (black contours; unit in hPa ; $\Delta = 2hPa$),
815 horizontal wind speed at 9 km altitude (black shadings; unit in ms^{-1} ; levels at 30, 40, 50, 60
816 ms^{-1}), and the mesoscale component of horizontal divergence at 12.5 km (blue contours,
817 positive; red contour, negative; contour levels at $\pm 7.5, \pm 15, \pm 30, \pm 60 \times 10^{-5} s^{-1}$) during RF02
818 in START08, with marked GV flight track (blue line) at selected time: (a) entire flight track at 21
819 April 18:00 UTC, (b) segment J1 at 21 April 19:10 UTC, (c) segment J2 at 21 April 19:50 UTC,
820 (d) segment J3 at 21 April 22:10 UTC, (e) segment M1 at 21 April 23:10 UTC, and (f) segment
821 M2 at 22 April 00:20 UTC. The triangle and circle marks represent the aircraft at the start time
822 of the segment and at selected time. The two-dimensional (2D) variables are based on D4 in Fig.
823 1. A band-pass filter is applied to extract signals with wavelength from 50 to 500 km for
824 horizontal divergence.

825

826 **Figure 3.** GV flight-level aircraft measurements during 5 selected segments (from left to right:
827 J1, J2, J3, M1 and M2) of RF02 in START08: (a) along-track velocity component (red; unit in
828 ms^{-1} ; left y axis), across-track velocity component (blue; unit in ms^{-1} ; right y axis) and
829 horizontal velocity component (black; unit in ms^{-1} ; left y axis), (b) vertical velocity component
830 (red; unit in ms^{-1} ; left y axis) and potential temperature (blue; unit in K ; right y axis), (c)
831 perturbation of hydrostatic pressure correction (red; unit in hPa ; left y axis), static pressure
832 (blue; unit in hPa ; right y axis) and corrected static pressure (black; unit in hPa ; left y axis), and
833 (d) flight height (red; unit in km ; left y axis) and terrain (blue; black shading below terrain; unit
834 in km ; right y axis). The series in segment J3 and M2 are reversed to facilitate the comparison
835 with J1+J2 and M1, respectively. Therefore, the orientation of x axis is from west to east along
836 each flight segment. The distance between minor tick marks in x axis is 100 km. The
837 perturbations in (c) are defined as the differences between the original data and their mean from
838 their corresponding segments.

839

840 **Figure 4.** The spectrum (black line) of GV flight-level aircraft measurement during 5 selected
841 segments (from left to right: J1, J2, J3, M1 and M2) of RF02 in START08: (a) along-track
842 velocity component (unit: $m^2s^{-2} \cdot m$), (b) across-track velocity component (unit: $m^2s^{-2} \cdot m$), (c)
843 vertical velocity component (unit: $m^2s^{-2} \cdot m$), (d) potential temperature (unit: $K^2 \cdot m$), and (e)
844 corrected static pressure (unit: $hPa^2 \cdot m$). Green lines show the theoretical Markov spectrum and
845 the 5% and 95% confidence curves using the lag 1 autocorrelation. The blue (red) reference lines
846 have slopes of $-5/3$ (-3).

847

848 **Figure 5.** Composite spectrum (black line) of GV flight-level aircraft measurement averaging
849 over all 68 segments in START08 (colored lines in Fig. 1): (a) along-track velocity component
850 (unit: $m^2s^{-2} \cdot m$), (b) across-track velocity component (unit: $m^2s^{-2} \cdot m$), (c) vertical velocity
851 component (unit: $m^2s^{-2} \cdot m$), (d) horizontal velocity component (unit: $m^2s^{-2} \cdot m$), (f) potential
852 temperature (unit: $K^2 \cdot m$), (g) corrected static pressure (unit: $hPa^2 \cdot m$), (h) static pressure
853 (unit: $hPa^2 \cdot m$), and (i) hydrostatic pressure correction (unit: $hPa^2 \cdot m$). The subplot (e) kinetic
854 energy (unit: $m^2s^{-2} \cdot m$) is the sum of (a)-(c). Green lines show the composite curves of the
855 theoretical Markov spectrum and the 5% and 95% confidence curves using the lag 1
856 autocorrelation. The blue (red) reference lines have slopes of $-5/3$ (-3).

857

858 **Figure 6.** Wavelet power spectrum of GV flight-level aircraft measurement during 5 selected
859 segments (from left to right: J1, J2, J3, M1 and M2) of RF02 in START08: (a) along-track
860 velocity component, (b) across-track velocity component, (c) vertical velocity component, (d)
861 potential temperature, and (e) corrected static pressure. Reference line (black line) shows the
862 cone of influence (COI), and the area outside COI is where edge error becomes important. Black
863 contour lines with dot shading represent 95% significance level based on a red noise background
864 (also see Torrence and Compo 1998; Woods and Smith 2010). The x axis is the same as in Fig.
865 3, including the reversal of segment J3 and M2.

866

867 **Figure 7.** The wavelet cospectrum of (a) $(u'w')_c$, (b) $(v'w')_c$, (c) $(p_c'w')_c$, (d) the quadrature
868 spectrum of $(\theta'w')_q$, and (e) the absolute coherence phase angle of $(\theta'w')_p$ for GV flight-level
869 aircraft measurement during 5 selected segments (from left to right: J1, J2, J3, M1 and M2) of
870 RF02 in START08. Reference line (black line) shows the cone of influence (COI), and the area

871 outside COI is where edge error becomes important. Black contour lines with dot shading
872 represent 95% significance level (also see Torrence and Compo 1998; Woods and Smith 2010).
873 The x axis is the same as in Fig. 3, including the reversal of segment J3 and M2. The horizontal
874 black line marks the scale of 50 km.

875

876 **Figure 8.** A relatively good/clean example of mesoscale variations during segment J3 (location
877 250-360 km): (a) along-track velocity component (red; unit in m/s) and vertical velocity
878 component (blue; unit in m/s), (b) across-track velocity component (red; unit in m/s) and vertical
879 velocity component (blue; unit in m/s), (c) along-track velocity component (red; unit in m/s) and
880 across-track velocity component (blue; unit in m/s), (d) corrected static pressure (red; unit in
881 hPa) and along-track velocity component (blue; unit in m/s), (e) corrected static pressure (red;
882 unit in hPa) and across-track velocity component (blue; unit in m/s), (f) corrected static pressure
883 (red; unit in hPa) and vertical velocity component (blue; unit in m/s), (g) potential temperature
884 (red; unit in K) and vertical velocity component (blue; unit in m/s), (h) static pressure (red; unit
885 in hPa) and vertical velocity component (blue; unit in m/s), and (i) hydrostatic pressure
886 correction (red; unit in hPa) and vertical velocity component (blue; unit in m/s). A wavelet-based
887 band-pass filter is applied to extract signals with wavelength from 100 to 120 km for all the
888 above flight variables.

889

890 **Figure 9.** Same as in Fig. 8, but for a relatively bad/noisy example of mesoscale variations
891 during segment J3 (location 560-688 km). The wavelet-based band-pass window is 118-138 km.

892

893 **Figure 10.** Same as in Fig. 8, but for a relatively good/clean example of smaller-scale variations
894 during segment J3 (location 650-750 km). The wavelet-based band-pass window is 32-64 km.

895

896 **Figure 11.** Same as in Fig. 8, but for an example of smaller-scale variations during segment J3
897 (location 680-780 km). The wavelet-based band-pass window is 8-16 km.

898

899 **Figure 12.** (a) The spectrum of corrected static pressure (black), static pressure (blue), and
900 hydrostatic pressure correction (red) based on GV flight-level aircraft measurement during 5
901 selected segments (from left to right: J1, J2, J3, M1 and M2) of RF02 in START08. (b) The
902 spectrum of the square root ratio (see the text for its definition).

903

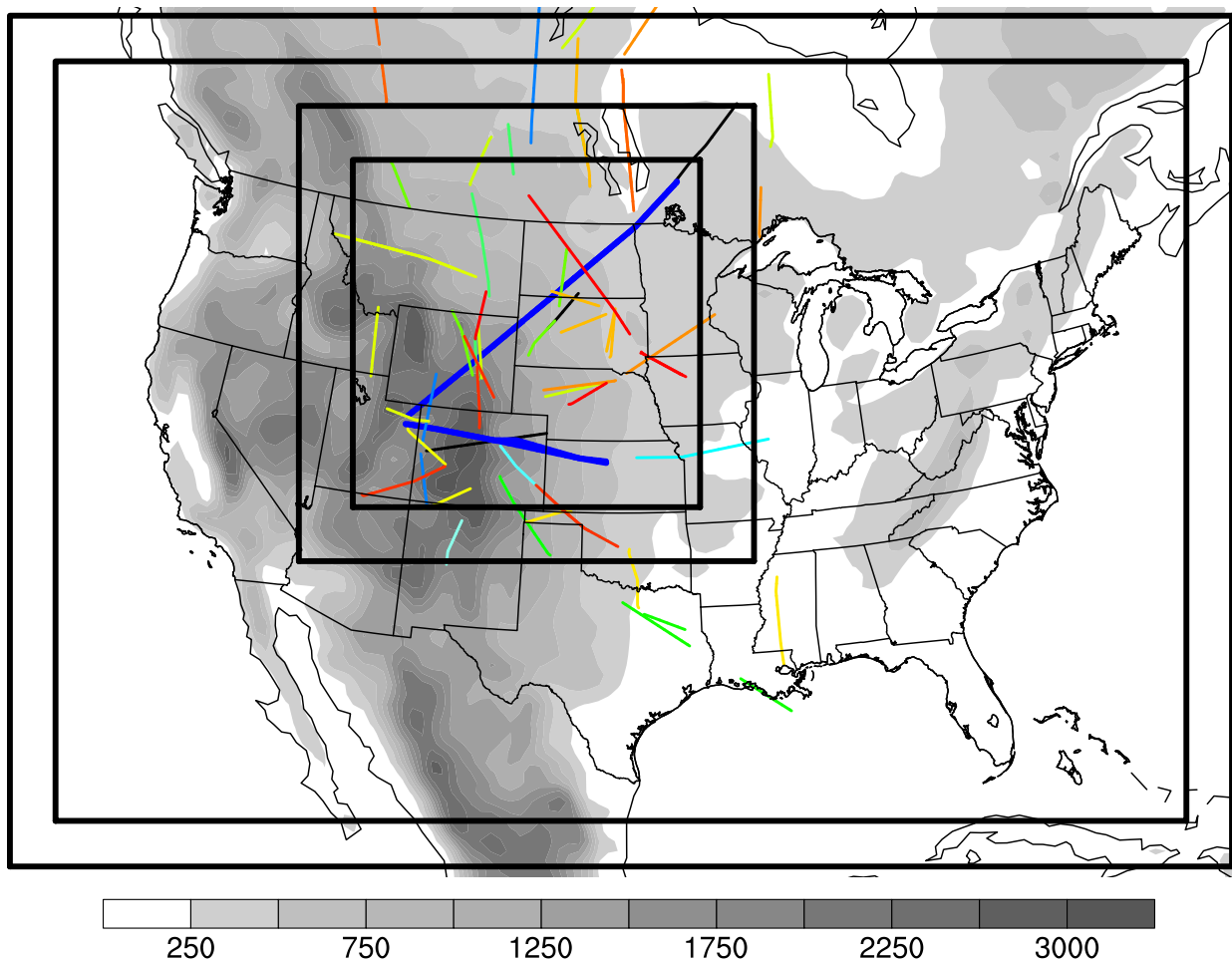
904

905 **Table 1:** The aircraft statistic parameters of five selected flight segment in RF02 during the
 906 START08 field campaign. Column 1-7 represent the name, the starting time (s), the ending time
 907 (s), the averaged flight height (km), the averaged static pressure (hPa), the total distance (km),
 908 and the averaged flight speed (m/s) of each selected flight segment.
 909

Flight Segment	Start (s)	End (s)	Averaged Flight Height (km)	Averaged Static Pressure (hPa)	Distance (km)	Averaged Flight Speed (m/s)
J1	2450	5000	11.8	196.9	685.74	268.92
J2	5170	8620	12.5	178.7	908.53	263.34
J3	9120	16850	13.1	162.1	1641.93	212.41
M1	17100	20630	12.6	178.5	950.46	269.25
M2	21500	26430	11.0	227.6	946.90	192.07

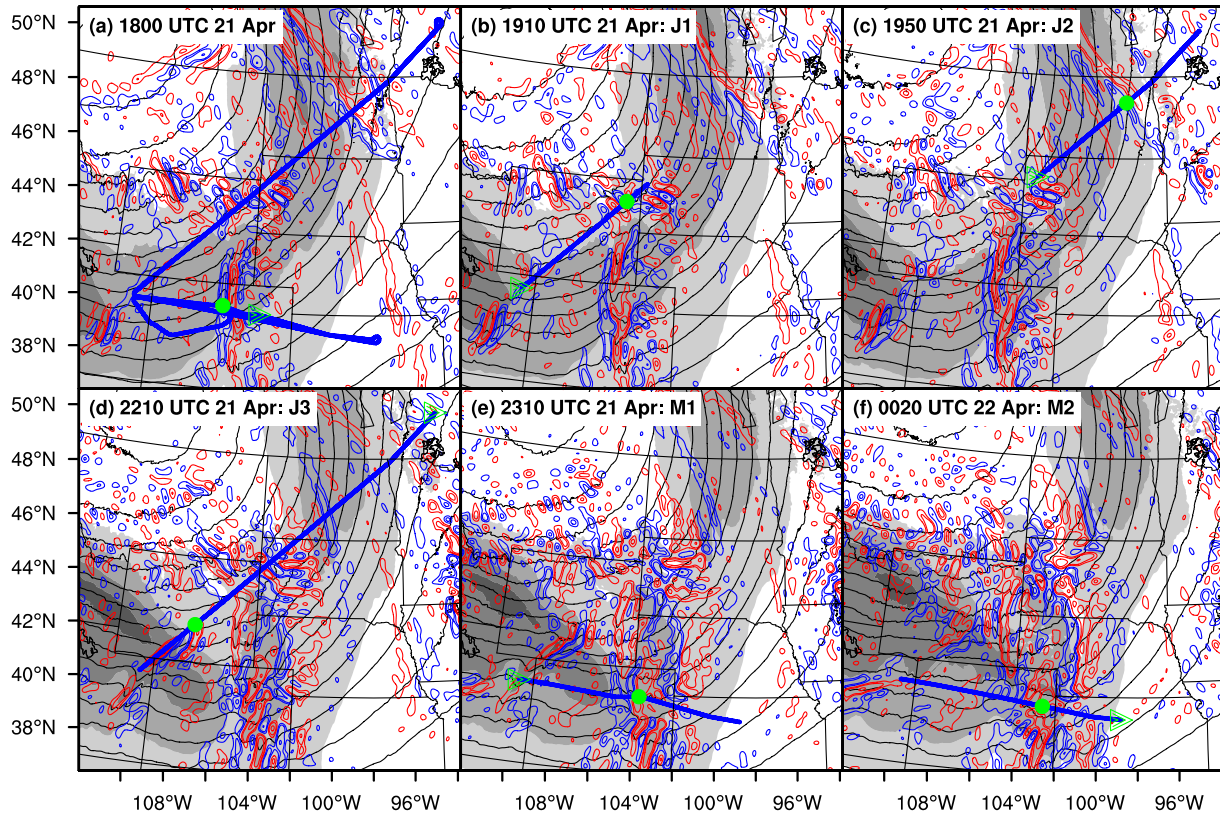
910

911



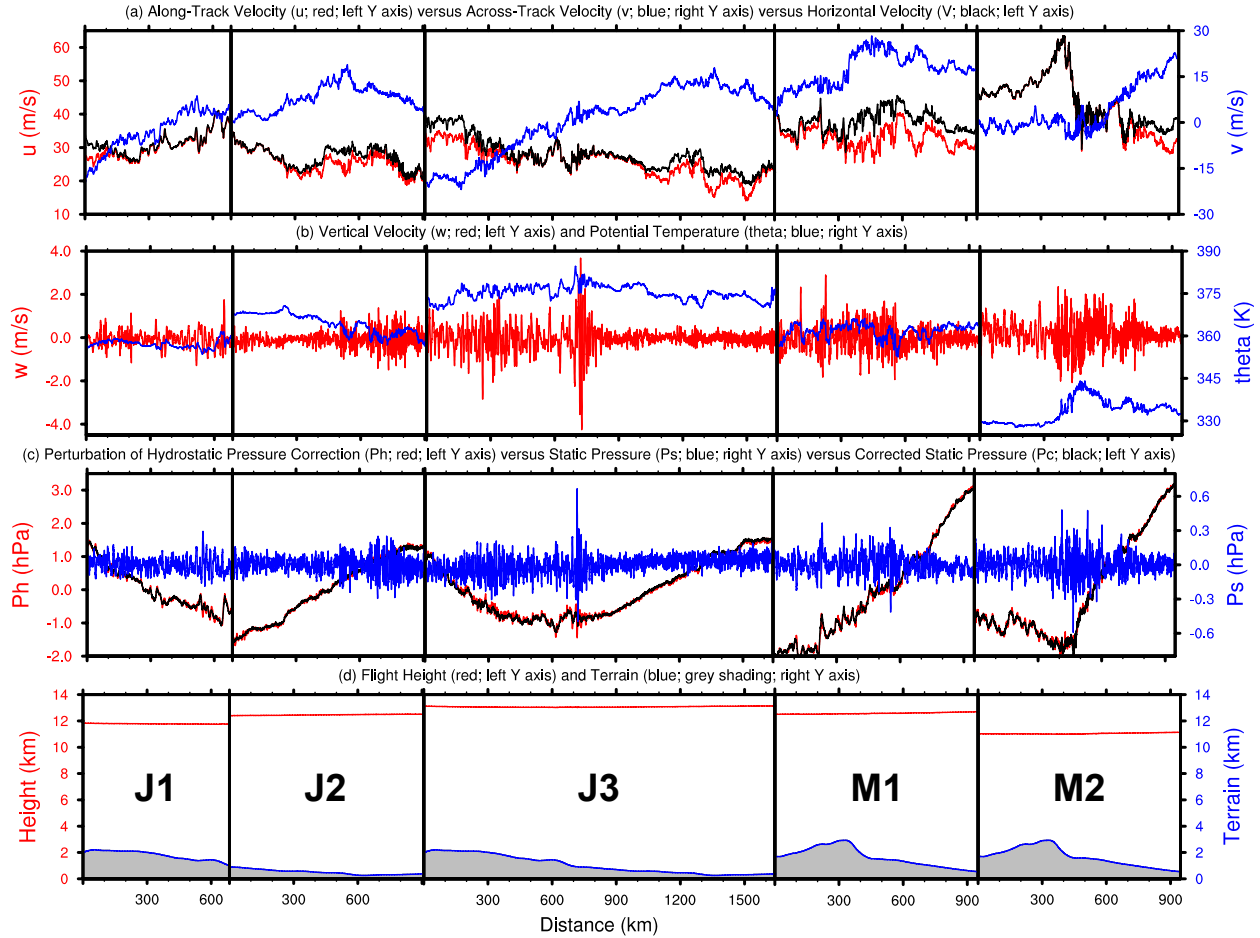
912

913 **Figure 1.** The 68 Gulfstream V (GV) flight segments (colored lines) selected for wave analysis
 914 during START08. The 18 colors represent 18 research flight (RF) missions. The thick blue lines
 915 represent the second flight (RF02). The grey shadings give the terrain elevation map (shaded
 916 every 250 m) over north America. The 4 black boxes are the model domain design for the second
 917 research flight (RF02) during 21-22 April 2008, which are named D1-D4 from coarse to fine
 918 domain with horizontal resolution as 45 km, 15 km, 5 km and 1.67 km, respectively. The field
 919 catalog of the 18 RFs are available online (at
 920 http://catalog.eol.ucar.edu/start_08/missions/missions.html). The GV ground tracks of the 18
 921 RFs are also documented in Fig. 2 of Pan et al. (2010).
 922



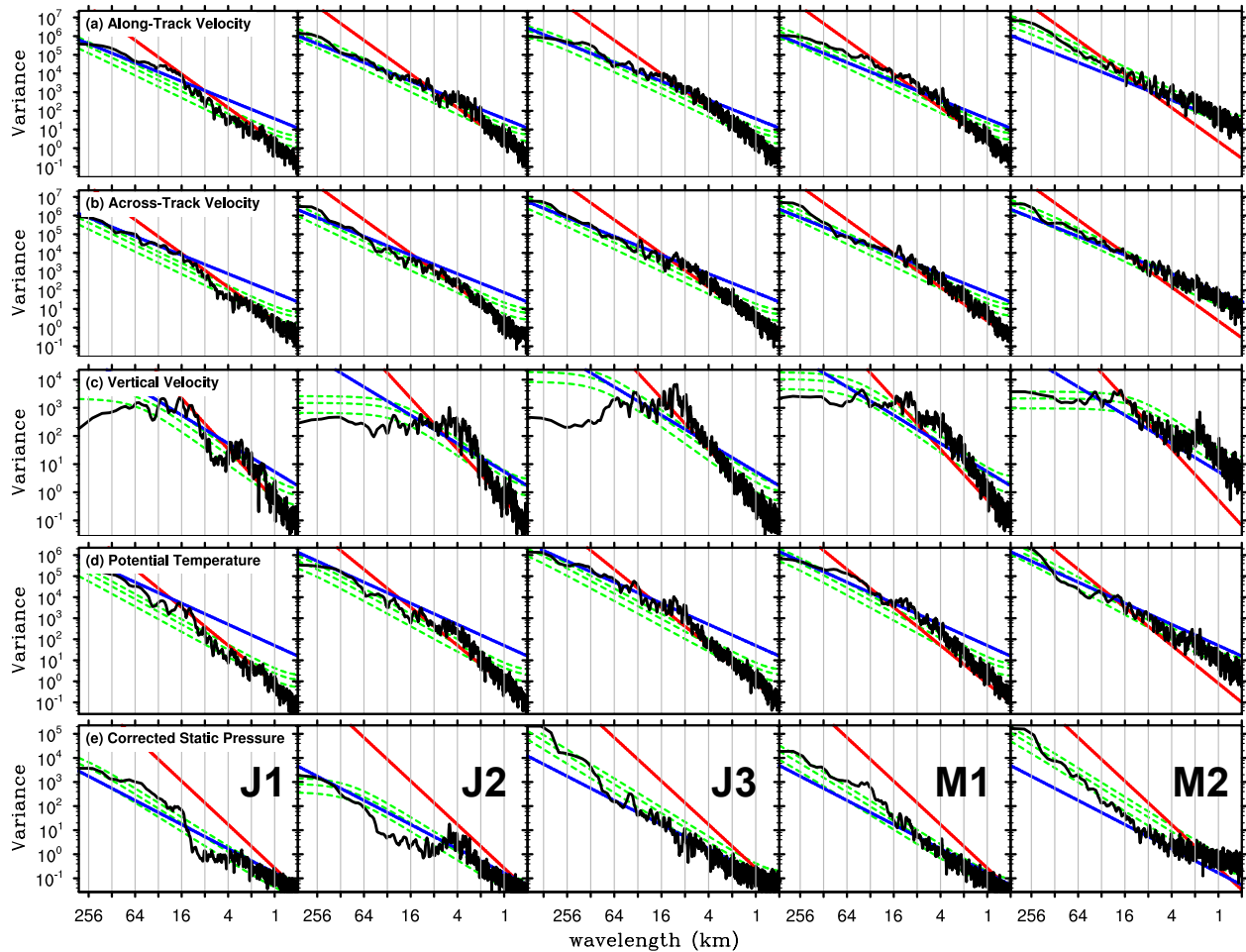
923
 924 **Figure 2.** Simulated pressure at 9 km altitude (black contours; unit in hPa ; $\Delta=2hPa$),
 925 horizontal wind speed at 9 km altitude (black shadings; unit in ms^{-1} ; levels at 30, 40, 50, 60
 926 ms^{-1}), and the mesoscale component of horizontal divergence at 12.5 km (blue contours,
 927 positive; red contour, negative; contour levels at $\pm 7.5, \pm 15, \pm 30, \pm 60 \times 10^{-5} s^{-1}$) during RF02
 928 in START08, with marked GV flight track (blue line) at selected time: (a) entire flight track at 21
 929 April 18:00 UTC, (b) segment J1 at 21 April 19:10 UTC, (c) segment J2 at 21 April 19:50 UTC,
 930 (d) segment J3 at 21 April 22:10 UTC, (e) segment M1 at 21 April 23:10 UTC, and (f) segment
 931 M2 at 22 April 00:20 UTC. The triangle and circle marks represent the aircraft at the start time
 932 of the segment and at selected time. The two-dimensional (2D) variables are based on D4 in Fig.
 933 1. A band-pass filter is applied to extract signals with wavelength from 50 to 500 km for
 934 horizontal divergence.

935



936

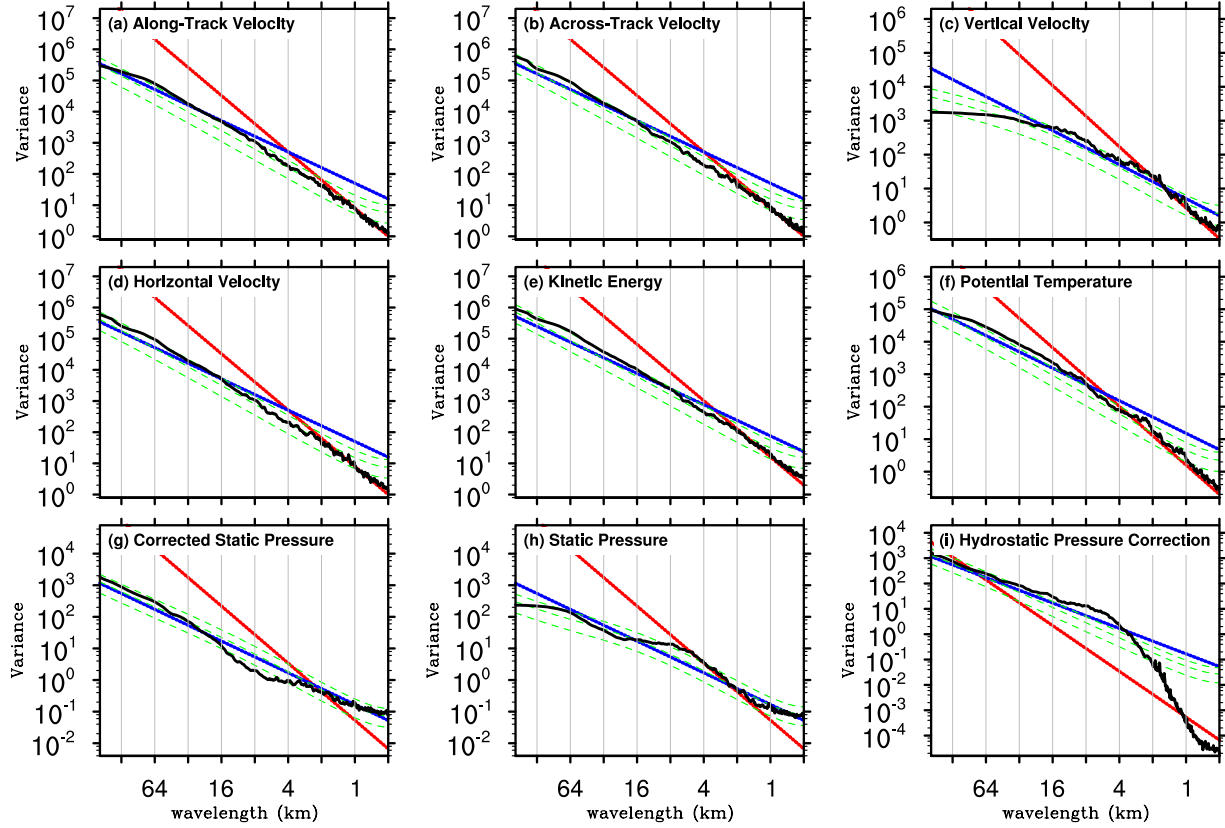
937 **Figure 3.** GV flight-level aircraft measurements during 5 selected segments (from left to right:
 938 J1, J2, J3, M1 and M2) of RF02 in START08: (a) along-track velocity component (red; unit in
 939 ms^{-1} ; left y axis), across-track velocity component (blue; unit in ms^{-1} ; right y axis) and
 940 horizontal velocity component (black; unit in ms^{-1} ; left y axis), (b) vertical velocity component
 941 (red; unit in ms^{-1} ; left y axis) and potential temperature (blue; unit in K ; right y axis), (c)
 942 perturbation of hydrostatic pressure correction (red; unit in hPa ; left y axis), static pressure
 943 (blue; unit in hPa ; right y axis) and corrected static pressure (black; unit in hPa ; left y axis), and
 944 (d) flight height (red; unit in km ; left y axis) and terrain (blue; black shading below terrain; unit
 945 in km ; right y axis). The series in segment J3 and M2 are reversed to facilitate the comparison
 946 with J1+J2 and M1, respectively. Therefore, the orientation of x axis is from west to east along
 947 each flight segment. The distance between minor tick marks in x axis is 100 km. The
 948 perturbations in (c) are defined as the differences between the original data and their mean from
 949 their corresponding segments.



950

951 **Figure 4.** The spectrum (black line) of GV flight-level aircraft measurement during 5 selected
 952 segments (from left to right: J1, J2, J3, M1 and M2) of RF02 in START08: (a) along-track
 953 velocity component (unit: $m^2s^{-2} \cdot m$), (b) across-track velocity component (unit: $m^2s^{-2} \cdot m$), (c)
 954 vertical velocity component (unit: $m^2s^{-2} \cdot m$), (d) potential temperature (unit: $K^2 \cdot m$), and (e)
 955 corrected static pressure (unit: $hPa^2 \cdot m$). Green lines show the theoretical Markov spectrum and
 956 the 5% and 95% confidence curves using the lag 1 autocorrelation. The blue (red) reference lines
 957 have slopes of $-5/3$ (-3).

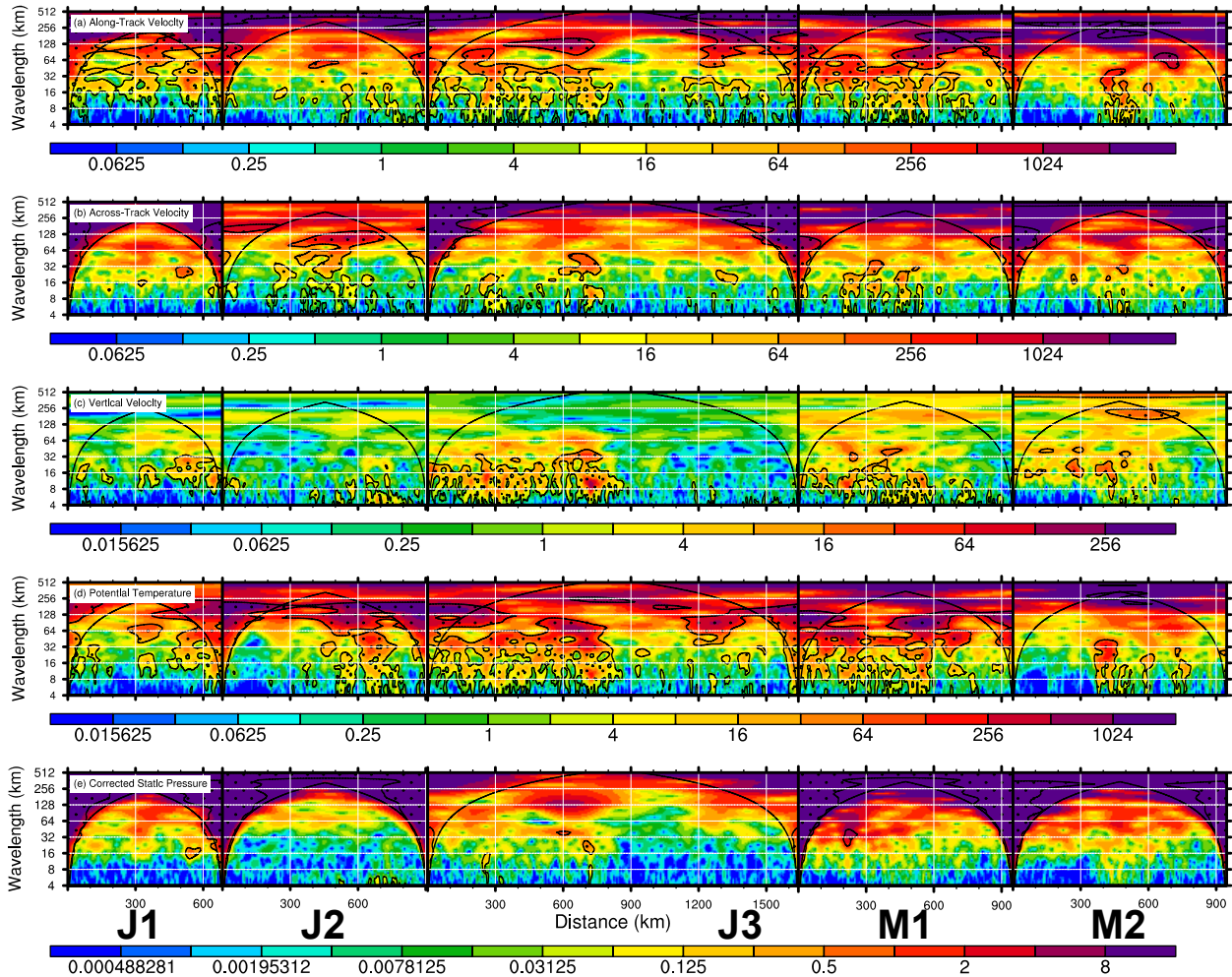
958



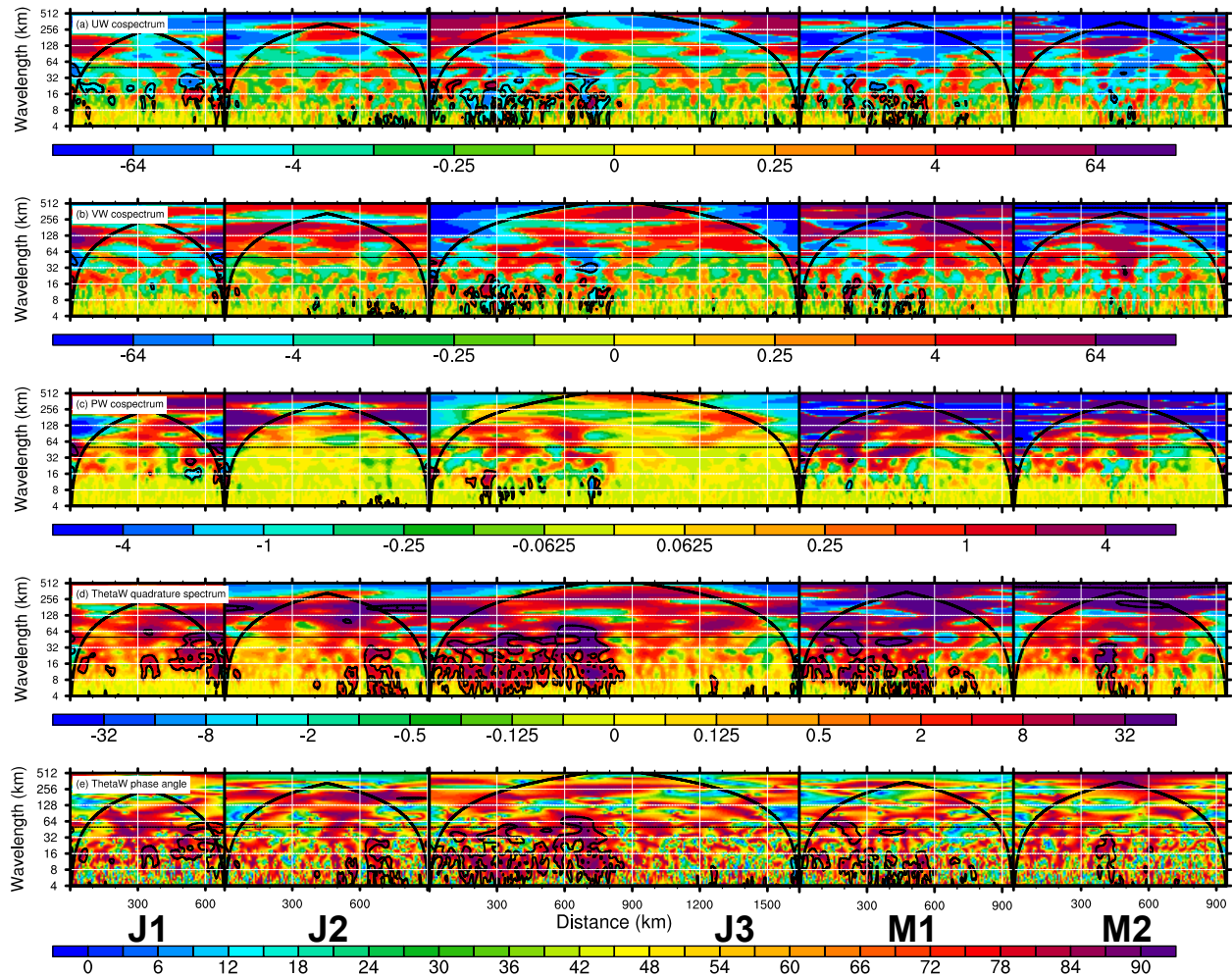
959

960 **Figure 5.** Composite spectrum (black line) of GV flight-level aircraft measurement averaging
 961 over all 68 segments in START08 (colored lines in Fig. 1): (a) along-track velocity component
 962 (unit: $m^2s^{-2} \cdot m$), (b) across-track velocity component (unit: $m^2s^{-2} \cdot m$), (c) vertical velocity
 963 component (unit: $m^2s^{-2} \cdot m$), (d) horizontal velocity component (unit: $m^2s^{-2} \cdot m$), (f) potential
 964 temperature (unit: $K^2 \cdot m$), (g) corrected static pressure (unit: $hPa^2 \cdot m$), (h) static pressure
 965 (unit: $hPa^2 \cdot m$), and (i) hydrostatic pressure correction (unit: $hPa^2 \cdot m$). The subplot (e) kinetic
 966 energy (unit: $m^2s^{-2} \cdot m$) is the sum of (a)-(c). Green lines show the composite curves of the
 967 theoretical Markov spectrum and the 5% and 95% confidence curves using the lag 1
 968 autocorrelation. The blue (red) reference lines have slopes of $-5/3$ (-3).

969



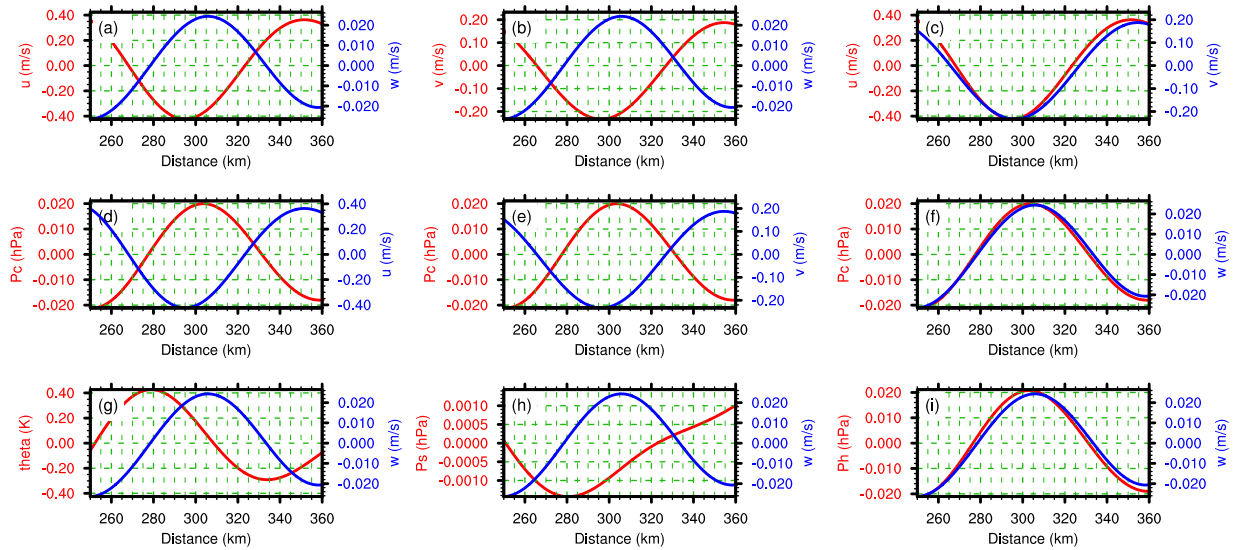
970
 971 **Figure 6.** Wavelet power spectrum of GV flight-level aircraft measurement during 5 selected
 972 segments (from left to right: J1, J2, J3, M1 and M2) of RF02 in START08: (a) along-track
 973 velocity component, (b) across-track velocity component, (c) vertical velocity component, (d)
 974 potential temperature, and (e) corrected static pressure. Reference line (black line) shows the
 975 cone of influence (COI), and the area outside COI is where edge error becomes important. Black
 976 contour lines with dot shading represent 95% significance level based on a red noise background.
 977 The x axis is the same as in Fig. 3, including the reversal of segment J3 and M2.
 978



979
 980
 981
 982
 983
 984
 985
 986
 987

Figure 7. The wavelet cospectrum of (a) $(u'w')_c$, (b) $(v'w')_c$, (c) $(p_c'w')$, (d) the quadrature spectrum of $(\theta'w')_q$, and (e) the absolute coherence phase angle of $(\theta'w')_p$ for GV flight-level aircraft measurement during 5 selected segments (from left to right: J1, J2, J3, M1 and M2) of RF02 in START08. Reference line (black line) shows the cone of influence (COI), and the area outside COI is where edge error becomes important. Black contour lines with dot shading represent 95% significance level. The x axis is the same as in Fig. 3, including the reversal of segment J3 and M2. The horizontal black line marks the scale of 50 km.

Segment J3 (distance: 250-360km; bandpass window: 100-120km)

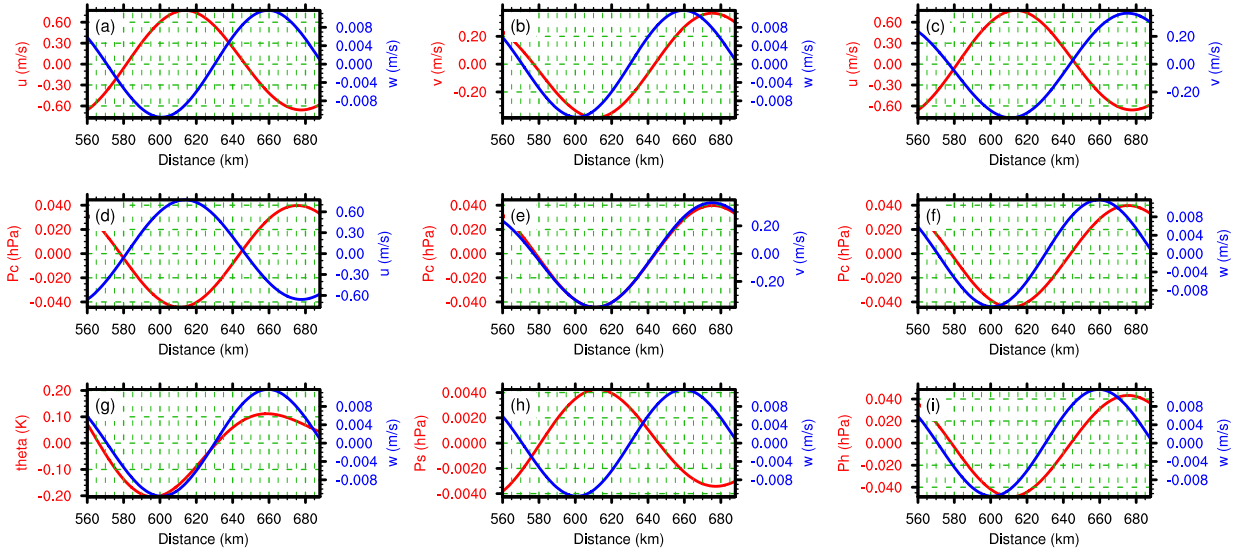


988

989 **Figure 8.** A relatively good/clean example of mesoscale variations during segment J3 (location
 990 250-360 km): (a) along-track velocity component (red; unit in m/s) and vertical velocity
 991 component (blue; unit in m/s), (b) across-track velocity component (red; unit in m/s) and vertical
 992 velocity component (blue; unit in m/s), (c) along-track velocity component (red; unit in m/s) and
 993 across-track velocity component (blue; unit in m/s), (d) corrected static pressure (red; unit in
 994 hPa) and along-track velocity component (blue; unit in m/s), (e) corrected static pressure (red;
 995 unit in hPa) and across-track velocity component (blue; unit in m/s), (f) corrected static pressure
 996 (red; unit in hPa) and vertical velocity component (blue; unit in m/s), (g) potential temperature
 997 (red; unit in K) and vertical velocity component (blue; unit in m/s), (h) static pressure (red; unit
 998 in hPa) and vertical velocity component (blue; unit in m/s), and (i) hydrostatic pressure
 999 correction (red; unit in hPa) and vertical velocity component (blue; unit in m/s). A wavelet-based
 1000 band-pass filter is applied to extract signals with wavelength from 100 to 120 km for all the
 1001 above flight variables.

1002

Segment J3 (distance: 560-688km; bandpass window: 118-138km)



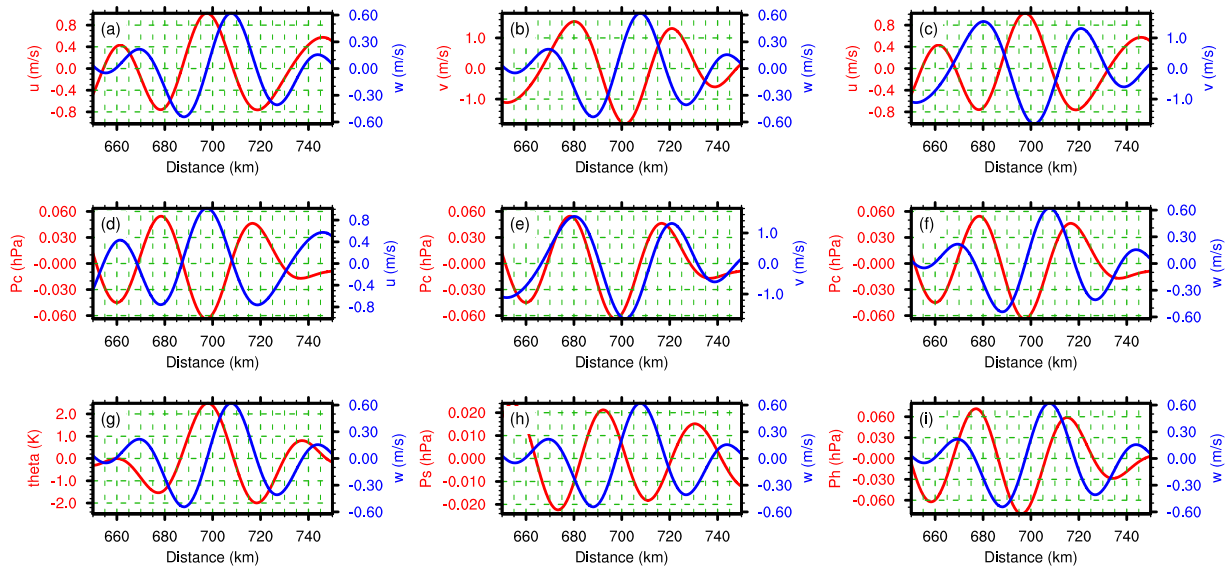
1003

1004 **Figure 9.** Same as in Fig. 8, but for a relatively bad/noisy example of mesoscale variations

1005 during segment J3 (location 560-688 km). The wavelet-based band-pass window is 118-138 km.

1006

Segment J3 (distance: 650-750km; bandpass window: 32-64km)



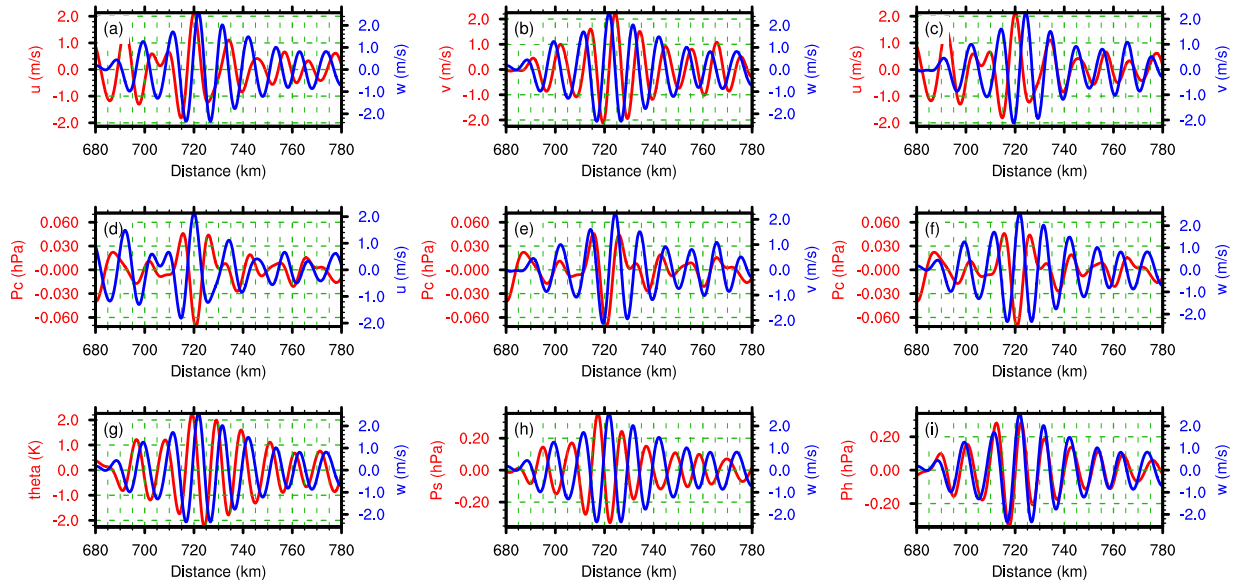
1007

1008 **Figure 10.** Same as in Fig. 8, but for a relatively good/clean example of smaller-scale variations

1009 during segment J3 (location 650-750 km). The wavelet-based band-pass window is 32-64 km.

1010

Segment J3 (distance: 680-780km; bandpass window: 8-16km)

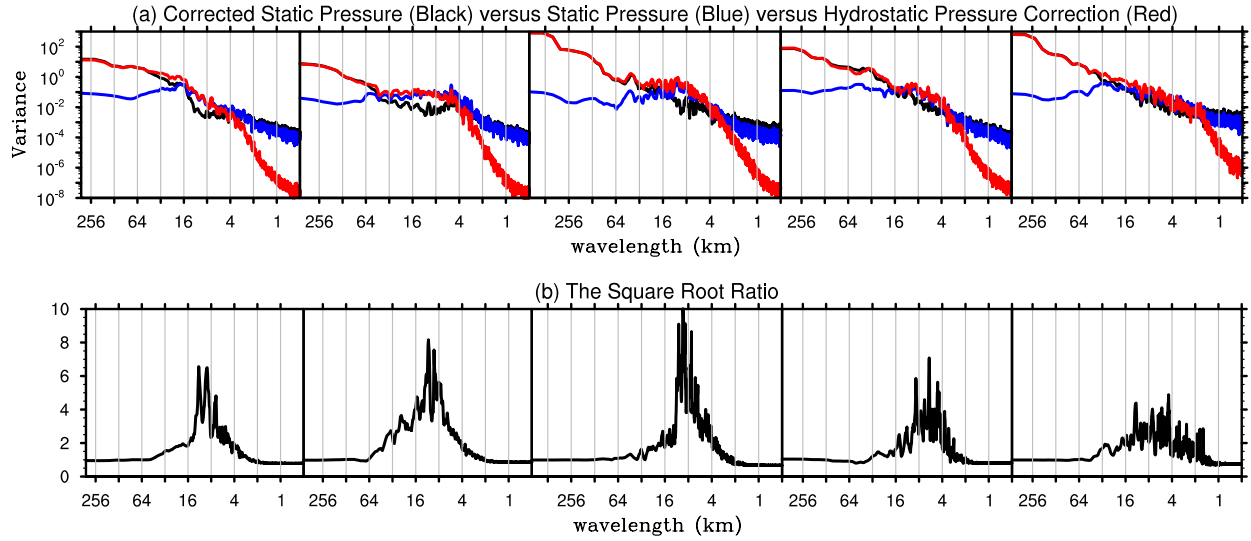


1011

1012 **Figure 11.** Same as in Fig. 8, but for an example of smaller-scale variations during segment J3

1013 (location 680-780 km). The wavelet-based band-pass window is 8-16 km.

1014



1015
 1016
 1017
 1018
 1019
 1020

J1 **J2** **J3** **M1** **M2**

Figure 12. (a) The spectrum of corrected static pressure (black), static pressure (blue), and hydrostatic pressure correction (red) based on GV flight-level aircraft measurement during 5 selected segments (from left to right: J1, J2, J3, M1 and M2) of RF02 in START08. (b) The spectrum of the square root ratio (see the text for its definition).